



## City Research Online

### City, University of London Institutional Repository

---

**Citation:** Almutairi, F., Tsavdaridis, K. D., Rodriguez, A., Asteris, P. & Lemonis, M. (2024). Hysteretic Behaviour of Composite Reduced Web Section (RWS) Connections for Seismic Applications. *Journal of Earthquake Engineering*, 28(2), pp. 349-384. doi: 10.1080/13632469.2023.2204172

This is the published version of the paper.

This version of the publication may differ from the final published version.

---

**Permanent repository link:** <https://openaccess.city.ac.uk/id/eprint/30345/>

**Link to published version:** <https://doi.org/10.1080/13632469.2023.2204172>

**Copyright:** City Research Online aims to make research outputs of City, University of London available to a wider audience. Copyright and Moral Rights remain with the author(s) and/or copyright holders. URLs from City Research Online may be freely distributed and linked to.

**Reuse:** Copies of full items can be used for personal research or study, educational, or not-for-profit purposes without prior permission or charge. Provided that the authors, title and full bibliographic details are credited, a hyperlink and/or URL is given for the original metadata page and the content is not changed in any way.



# Hysteretic Behaviour of Composite Reduced Web Section (RWS) Connections for Seismic Applications

Fahad Falah Almutairi<sup>a</sup>, Konstantinos Daniel Tsavdaridis<sup>b</sup>, Andres Alonso Rodriguez<sup>c,d,e</sup>, Panagiotis G. Asteris<sup>f</sup>, and Minas E. Lemonis<sup>f</sup>

<sup>a</sup>School of Civil Engineering, Faculty of Engineering and Physical Sciences, University of Leeds, Leeds, UK; <sup>b</sup>Department of Civil Engineering, School of Mathematics, Computer Science and Engineering, City, University of London, London, UK; <sup>c</sup>Institute for Risk and Uncertainty, University of Liverpool, Liverpool, UK; <sup>d</sup>Department of Civil Engineering, Catholic University of the North, Antofagasta, Chile; <sup>e</sup>Faculty of Environment, Science, and Economy, University of Exeter, Exeter, UK; <sup>f</sup>Computational Mechanics Laboratory, School of Pedagogical and Technological Education, Heraklion, Athens, Greece

## ABSTRACT

Whilst there has been research about reduced web section beams; RWS, their seismic behaviour when they are overlaid by slabs is not well understood. This study addresses this by assessing a high-definition finite element representation of non-seismically detailed RWS connections with slabs. The composite action is investigated, focusing on effects of the size and location of the web openings. These connections can reach a 4% interstorey drift, thus comprising special moment frames in accordance with AISC 341. Moreover, beam, column, and joint tearing were avoided entirely, and at the most, brittle failure of bolts in the end plate was observed.

## ARTICLE HISTORY

Received 14 June 2022  
Accepted 11 April 2023



## KEYWORDS

Steel seismic design; reduced web section connection; seismic retrofit of steel structures; capacity design

## 1. Introduction

Joint beam-slab action can lead to changes in the expected yield mechanism of beam-column connections when subjected to cyclic actions. Particularly, a non-symmetric yield moment occurs. When tension is observed on the slab, the moment capacity increases due to deformation of the steel rebar. Then, behavior changes completely when the moment reverses and compression is induced on the slab, leading to extensive deformation of the beam bottom flange. These extreme strain reversals can lead to early buckling of bottom flanges and damage to the beam-slab connection; whilst increased yielding moment capacity leads to higher strength demands on elements outside the protected zones; which are locations where yielding is encouraged, leading to the development of structural fuses. Hence, they are also known as plastic zone/structural fuses. The most critical issues induced by this are failure of welds and bolts in endplates, buckling of endplates, and yielding and tearing of the panel zone or columns. All of these phenomena are undesired non-ductile failure modes (Lee et al. 2016; Shaheen, Tsavdaridis, and Yamada 2018; Sumner 2003). However, total decoupling of slabs and underlying beams is not always feasible as composite action significantly increases moment capacity and reduces deflections at midspan, which is required for supporting gravity loading and preventing damage to non-structural elements due to sagging.

Thus, there has been extensive research on the behaviour of beam-slab composite actions in conventional welded steel moment connections and reduced beam section (RBS) connections (Chen and Chao 2001; Kim and Lee 2017; Lee et al. 2016; Shaheen, Tsavdaridis, and Yamada 2018; Sumner 2003). In overall terms, it has been found that composite action persists even when there is extensive

**CONTACT** Andres Alonso Rodriguez  [a.alonso-rodriguez@exeter.ac.uk](mailto:a.alonso-rodriguez@exeter.ac.uk)  Institute for Risk and Uncertainty, Faculty of Environment, Science and Economy, University of Exeter, Hope Hall, 1.21, Exeter EX4 4PL, UK

© 2023 The Author(s). Published with license by Taylor & Francis Group, LLC.

This is an Open Access article distributed under the terms of the Creative Commons Attribution License (<http://creativecommons.org/licenses/by/4.0/>), which permits unrestricted use, distribution, and reproduction in any medium, provided the original work is properly cited. The terms on which this article has been published allow the posting of the Accepted Manuscript in a repository by the author(s) or with their consent.

crushing and cracking in the slab (Chen and Chao 2001; Landolfo et al. 2017; Lee et al. 2016; Shaheen, Tsavdaridis, and Yamada 2018; Shin et al. 2017a). Sumner and his collaborators (Sumner, Mays, and Murray 2000a, 2000b) studied ways to prevent undesired coupled beam-slab action near connections, finding that the best solution is decoupling their joint action in that place whilst preserving it at midspan. This can be accomplished by suppressing beam shear studs in the protected zone, and by allowing for a gap between the column and the slab. Laboratory testing has validated summer's approach (Civjan, Engelhardt, and Gross 2000, 2001; Jones, Fry, and Engelhardt 2002; Lee et al. 2016; Sumner, Mays, and Murray 2000a, 2000b; Zhang and Ricles 2006a, 2006b) and found that damage to the beam is reduced, while structural demands outside the protected zone are mitigated, even leading to a significant reduction of slab cracking (Lee et al. 2016). Moreover, if there is a monolithic connection between the column and the slab, slab tearing and cracking can be reduced by avoiding shear connections close to the beam-column interface (Zhang and Ricles 2006a, 2006b).

Reduced Web Beams (RWS) have become mainstream in regions where seismic hazard is low, leading to design guidelines for their use to support static loads (Lawson and Hicks 2011). RWS involves the provision of perforations in the beam web to lower self-weight and ease installation of utilities within ceilings. The most common yielding mode of RWS connections is through the Vierendeel mechanism, which involves local yielding at the edges of the perforations, thus capping shear transfer across the beam. As the Vierendeel mechanism allows for large deformations in the inelastic range, there is potential for using RWS connections to endure earthquake actions. This has led to research about the behaviour of RWS connections when subjected to cyclic actions (Davarpanah et al. 2020; Erfani and Akrami 2017; Erfani, Akrami, and Mohammad-Nejad 2020; Shin et al. 2017a, 2017b; Tabar, Alonso-Rodríguez, and Tsavdaridis 2022; Tsavdaridis, Faghih, and Nikitas 2014; Tsavdaridis, Lau, and Alonso-Rodríguez 2021; Yang, Li, and Yang 2009; Zhang, Zheng, and Zhao 2019). Results of numerical simulations have shown that RWS is capable of ductile yielding through the Vierendeel mechanism without crippling out-of-plane buckling (Boushehri, Tsavdaridis, and Cai 2019; Erfani and Akrami 2017; Li, Yang, and Yang 2011; Momenzadeh, Kazemi, and Asl 2017; Naughton et al. 2017; Nazaralizadeh et al. 2020; Tsavdaridis and Papadopoulos 2016; Tsavdaridis, Faghih, and Nikitas 2014; Yang, Li, and Yang 2009). Thus, they offer a competitive solution for retrofitting of buildings, as making perforations on the beam web can be done with relative ease from the floor below; whilst strengthening the beam-column connection using supplementary plates or trimming of flanges for making in-situ RBS connections would be highly disruptive because that course of action requires partial demolition of floors overlaid on the beams.

Currently, there is little research about the interaction of slabs and RWS connections (Bi et al. 2021; Shaheen, Tsavdaridis, and Yamada 2018). Solutions addressed previously involve a single opening close to the connection, or the use of castellated beams, which have hexagonal perforations. Hence, previous studies considered few perforation and beam configurations. This paper addresses this knowledge gap by studying this phenomenon through parametric, high-definition numerical simulations of 48 specimens with a single circular perforation and different shear transfer stud configurations. Furthermore, the methodology has been benchmarked by reproducing laboratory tests on other structural engineering solutions, indicating that the results obtained are reliable. This work uncovers the effects of interaction between slabs and overlaid RWS connections and explores ways to adapt Summer's approach to RWS-slab composite structural systems.

## 2. Overview of Reduced Web Section (RWS) Connections

RWS connections make use of beams with perforations in their webs, to reduce self-weight and ease installation of utilities through the perforations. For new buildings, they are usually ensembled by welding together two-half tee sections of the same or different W profiles, effectively doubling the structural depth of the ensemble whilst minimizing waste. When used for structural retrofitting, the most convenient course of action is cutting holes directly in the webs, and in most cases, perforations are done solely close to beam-column joints. Therefore, the most usual, final configuration with and without a slab is depicted in Fig. 1.



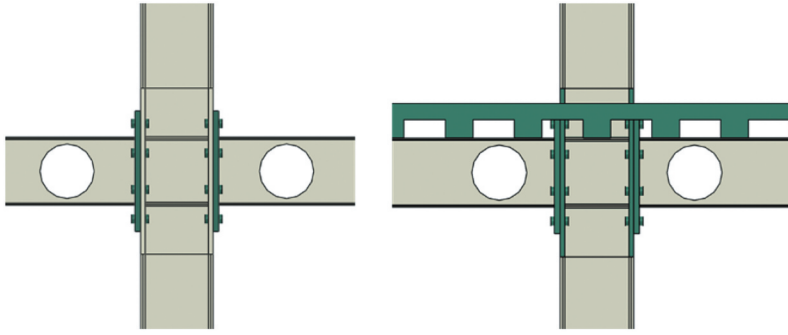


**Figure 1.** Reduced web section (RWS) connection.

Yielding usually starts in the corner of the perforations and eventually leads to the formation of a plastic Vierendeel mechanism when four plastic hinges are developed, as shown in Fig. 2. Also, it is possible to observe concurrent yielding of the minimal cross-section; particularly when joint slab-beam action is avoided. Both yielding mechanisms allow for extensive rotation ductility if local buckling and torsion are controlled. Moreover, the Vierendeel mechanism limits the shear along the beam, thus capping demands outside protected zones (Boushehri, Tsavdaridis, and Cai 2019; Erfani and Akrami 2017; Guo et al. 2011; Li, Yang, and Yang 2011; Naughton et al. 2017; Tsavdaridis, Faghih, and Nikitas 2014; Tsavdaridis, Lau, and Alonso-Rodríguez 2021; Yang, Li, and Yang 2009; Zhang, Zheng, and Zhao 2019).

There is significantly less research on the behaviour of the interaction of RWS connections and their overlying slabs. Research on beams with circular and hexagonal perforations (Bi et al. 2021; Shaheen, Tsavdaridis, and Yamada 2018) indicates that there is a noticeable increase in moment capacity when tension is observed on the slab, which can be up to 25% larger than without the slab. This value is close to what has been accounted for in other composite flooring systems, and thus decoupling beam and slab response by suppressing shear transfer studs could be a reasonable course of action (ANSI/AISC 341-16 2016; ANSI/AISC 358-16 2016; Eurocode 2005d). Previous studies (Civjan, Engelhardt, and Gross 2000, 2001; Jones, Fry, and Engelhardt 2002; Lee et al. 2016; Sumner, Mays, and Murray 2000a, 2000b; Zhang and Ricles 2006a, 2006b) indicate that this approach mitigates strength degradation and strains generated on the beam bottom flange at the column face; and avoids fracture at the beam's bottom flange. Also, it alleviates slab crushing and cracking in the vicinity of the column.

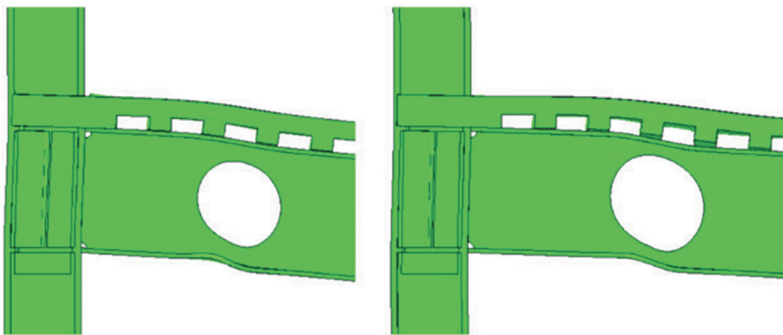


**Figure 2.** Vierendeel Mechanism (Shaheen, Tsavdaridis, and Yamada 2018).

### 3. Methodology

This study aims to increase our understanding of the behaviour of the joint slab-beam action of RWS connections with single openings in the vicinity of beam-column joints. This is achieved by formulating parametric high-resolution finite element models in Abaqus®, to represent with detail the interaction of all structural elements in the beam-column connection, focusing on the protected zone. The Finite element model is benchmarked firstly by reproducing results of an experimental campaign performed in beams without perforations (Chaudhari 2017; Chaudhari et al. 2019). After finding close agreement with laboratory results, 48 different models were analyzed. These models studied different configurations with varying hole diameter ( $d$ ), hole spacing from the column face and inclusion of shear studs to ensure effective coupling of the beam and the slab. Also, models without studs were assessed to explore the advantages of slab decoupling in the protected zone.

#### 3.1. Modelling of Beam-Slab Coupling

The behaviour of bolted extended end-plate connections under cyclic loading is complex as it involves several phenomena. Firstly, there is sliding and friction through the slab-beam and on the bolt-slab interfaces. Also, there are secondary effects arising from bolt precompression; elongation (Morrison, Schweizer, and Hassan 2016; Nazaralizadeh et al. 2020); buckling and, cracking as cyclic loads are imposed. Thus, there is widespread variability in the detail on how bolt behaviour is represented in numerical models. For example, it is a common practice to simplify the geometry of bolts in coupled beam-column connections by considering hexagonal or rectangular shapes instead of circles (Díaz et al. 2011; ElSabbagh et al. 2019; Lim, Choi, and Sumner 2012; Mashaly et al. 2011). Other researchers put great detail on their idealization, considering their true cross-section while explicitly representing their elongation and the diminishing in the in-plane cross-section due to transversal deformation, quantified by the Poisson coefficient in homogeneous materials (ElSabbagh et al. 2019; Gerami et al. 2011; Lam and Fu 2005; Lim, Choi, and Sumner 2012; Morrison, Quayyum, and Hassan 2017; Sofias, Kalfas, and Pachoumis 2014). Also, there are some cases of steel-concrete composite bolted extended end-plate connections where bolts and plates are considered to deform monolithically (Gil, Goñi, and Bayo 2013; Lam and Fu 2005; Vasdravellis, Valente, and Castiglioni 2009; Wang 2010). Regarding the interface, high-resolution models use a combination of shell and solid elements to model the beam-column joint elements (Sofias, Kalfas, and Pachoumis 2014). This requires detailed rules for matching node behaviour on distinct types of elements, involving tribology laws that allow for effects of bolt prestress, and non-linear joint deformation (ElSabbagh et al. 2019; Gerami et al. 2011; Morrison, Quayyum, and Hassan 2017; Sofias, Kalfas, and Pachoumis 2014).

The focus of this research has been on assessing the composite behaviour while enduring monotonic loads, thus representing static actions (Gil, Goñi, and Bayo 2013; Lam and Fu 2005; Vasdravellis, Valente, and Castiglioni 2009; Wang 2010). Research considering reversible, cyclic actions is sparse (Chaudhari 2017; Wang et al. 2018) and not as detailed. For example, Chaudhari (2017) didn't include the end-plate in their FE models. Nevertheless, there is good agreement between numerical simulations and test results for both cyclic and monotonic actions.

#### 3.2. Model Description

This study considers a cruciform arrangement to test the structural capacity of the RWS column connection. The cruciform arrangement allows for a direct estimation of the drift capacity of beam-column connections and represents closely the behavior of an inner joint in a multi-storey frame (Standards New Zealand 2007).

Furthermore, benchmarking of the finite element model is done by replicating results obtained by Chaudhari (2017), Chaudhari et al. (2019) by testing a bare steel joint (BSF) and a steel full-section beam-concrete composite slab. Both types of specimens employed extended end-plate connections, as

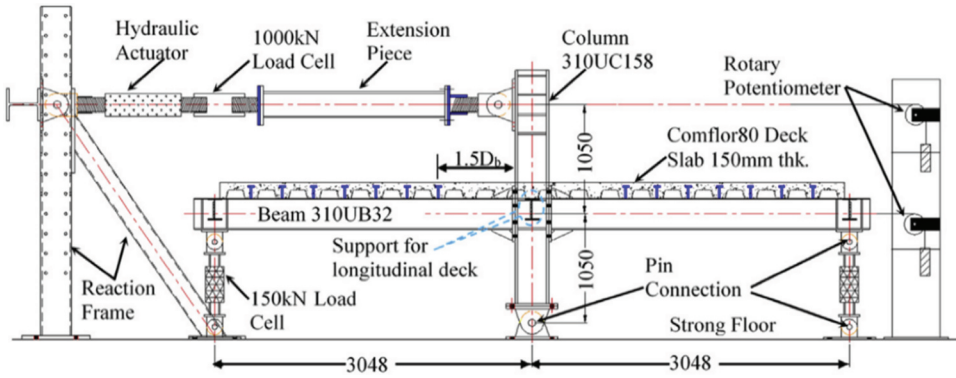


Figure 3. Elevation of test setup (Chaudhari 2017; Chaudhari et al. 2019).

shown in Fig. 3. Detailing of the connection was done in accordance with the NZ3404 standards (Standards New Zealand 2007). Continuity plates were welded on both sides of the column. The 25 mm extended end-plate connections include four rows of two bolts (M24 class 8.8) that were subjected to a prestress tension of 212 kN. The thicknesses of rib stiffeners and continuity plates were 12 mm and 16 mm, respectively. The boundary and loading conditions employed in FE models simulated the ones in the experimental tests. The ACI loading protocol (ACI 2005) considering displacement control was applied, as illustrated in Fig. 4. Eigen buckling analyses were initially performed to introduce a geometric imperfection. As suggested in (Tsavdaridis and D'Mello 2009), the first shape of Eigenmode was selected and scaled by the recommended factor of  $t_w/200$ . The low composite action was achieved by avoiding shear transfer studs for a distance from the column spanning 1.5 times the beam depth, while allowing for a 25 mm gap between the steel elements and the concrete slab, as shown in Fig. 3.

### 3.3. Constitutive Laws

Steel was modelled considering a bilinear stress-strain relationship with adaptative parameters that represent a combined isotropic and kinematic hardening – material, in accord with the formulation implemented in Dassault Systemes (2014). This material was allocated to the main steel structural elements (beam, column, and extended end-plate) as shown in Fig. 5a,b. The unitary strain for which the peak stress is observed  $\epsilon_u$ , was set to be equal to 15 times the yield unitary strain,  $\epsilon_y$ . Whilst the strain at which fracture is observed  $\epsilon_r$  was set up at 10 times  $\epsilon_u$  in accord with (Díaz et al. 2018). A value of  $\epsilon_u$  equal to 0.05 was enforced for bolts, as fracture is considered to happen upon achievement of peak resistance. The concrete slab was modelled using a concrete damaged plasticity (CDP) model based on the constitutive law presented in Eurocode 2 (2004) and the exponential tension softening model (Cornelissen, Hordijk, and Reinhardt 1986). The stress-strain relation for the normal concrete

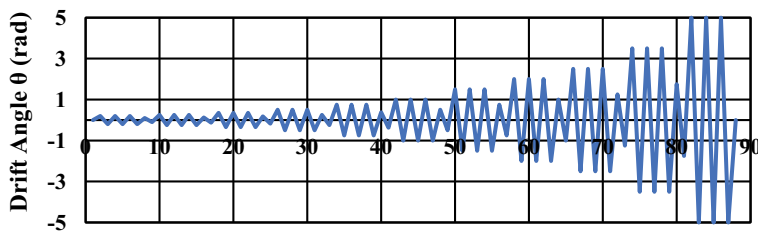
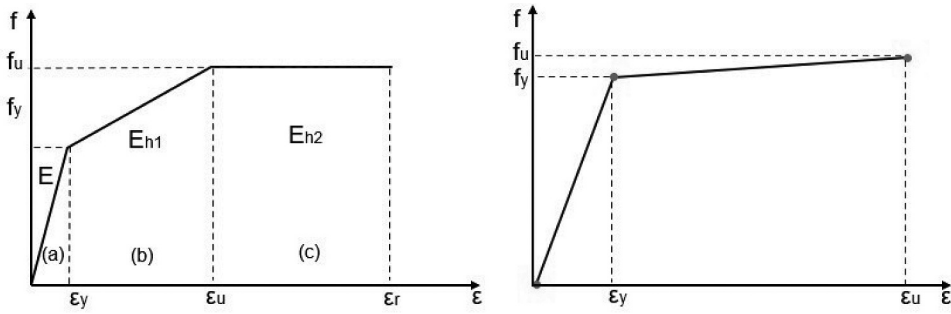
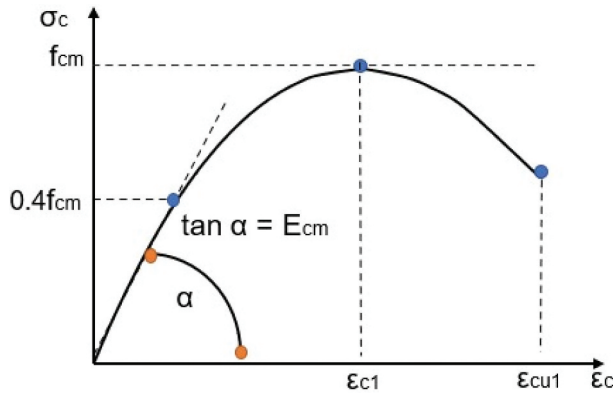


Figure 4. Displacement control loading regime of ACI report T1.1-01 (ACI 2005).



**Figure 5.** Material stress-strain curve for beam, column and connection (Chaudhari 2017; Chaudhari et al. 2019).



**Figure 6.** Schematic representation of the stress-strain curve for structural analysis (Eurocode 2004).

compression behaviour is defined in Eurocode 2 (2004) by an equivalent uniaxial stress-strain curve as shown in Fig. 6. A number of models can be used to express the tension-softening behaviour of normal concrete, such as linear, bilinear, and exponential. The exponential model was adopted (Fig. 7) as it has been judged to be the most practical realistic model, in accordance with results obtained by Cornelissen, Hordijk, and Reinhardt (1986), and further details are available in Ahmed and Tsavdaridis (2022). An elastic-perfectly-plastic model was adopted for steel elements outside the panel zone and for rebar. Nominal properties were considered for all materials, as assessing the effects of variability during manufacturing is out of the scope of this study.

### 3.4. Characteristics of the Finite Element Model

The concrete slab, the panel zone, bolts, end plates, and shear studs were modeled using 8-node solid elements with reduced integration (element-type C3D8R). Beams, stiffeners, and top and bottom parts of the column were modelled using 4-node shell elements with reduced integration (S4R) as shown in Fig. 8. This modeling technique of using a combination of 3D shell and 3D solid elements was adopted to increase accuracy in simulating the behavior of the steel-concrete composite bolted extended end-plate whilst decreasing computation time and memory usage, compared to what would be required if all elements were modelled as solids. Reinforcement steel bars were represented using truss elements (2-node linear, T3D2); as they can only endure uniaxial tension and compression. The metal deck was not modelled because it is used mainly as formwork for placement of concrete, whereas its inclusion would increase the complexity of the model without aggregated value; as the absence of metal decking affects the pattern of cracks in

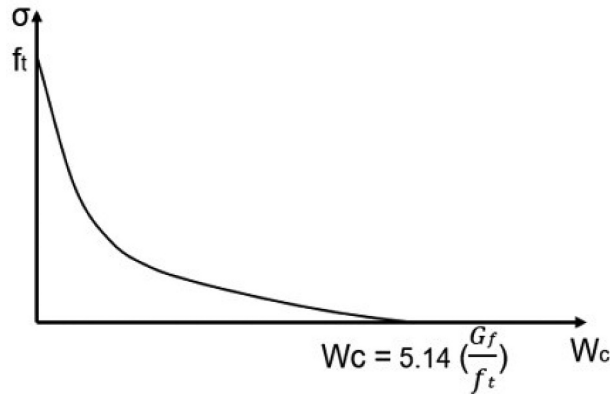


**Figure 7.** Exponential tension softening (Ahmed and Tsavdaridis 2022).

the concrete slab but not the structural capacity of connection (Darwin and Donahey 1988; Shaheen, Tsavdaridis, and Yamada 2018). This is explained by the fact that the interaction of shear studs (number of shear studs) with the concrete slab is the most critical factor that governs the capacity of the connection, instead of allocation of the steel deck, which acts primarily as workform (Darwin and Donahey 1988; Shaheen, Tsavdaridis, and Yamada 2018). Furthermore, the inclusion of metal decking in the model may lead to numerical instabilities that could end in the early termination of the analysis (Baskar, Shanmugam, and Thevendran 2002).

A mesh sensitivity analysis was conducted using various mesh sizes to evaluate the calculation time, storage, and accuracy of the results. Based on the mesh sensitivity analysis as displayed in Figs. 9 and 10, the element size ranged between 30 mm for steel and 35 mm for slab, which is enough to capture the effects of stress concentration features that are observed during laboratory testing (Chaudhari et al. 2019). The element size of the bolts and shear studs were 15 mm and 6 mm, respectively. This resolution provides close agreement with experimental results, but with a significant reduction in time and computing resources, as shown in Figs. 9 and 10. Interactions among diverse elements are in accordance with one of the following approaches:

- (1) The constraints (equal displacements) used to simulate the welding between steel elements were applied.
- (2) Normal and tangent interactions considering hard contact and a friction coefficient equal to 0.2, which corresponds to the case of untreated-rolled surfaces (Chaudhari 2017; Eurocode 2005a) was adopted whilst allowing for finite sliding to simulate contact among steel elements.
- (3) Frictionless normal and tangent interactions with displacement control to simulate steel-concrete contact were used.
- (4) Embedded elements for the interaction of concrete, rebar, and tie studs within the slab were utilized.

#### 4. FEM Benchmarking

The proposed numerical model is capable of reproducing well the displacement-load hysteresis curves of both benchmarking experiments (Chaudhari 2017; Chaudhari et al. 2019). Behaviour before yielding, stiffness degradation, and hysterical energy dissipation are closely simulated as differences between-load-story drift ordinates diverge by less than 6% for the model without a slab (BSF); while becoming less than 4% for the model with a slab (FI) as shown in Fig. 11. In addition, the model captures well-residual deformations, and yield and failure modes. Particularly, it reproduces closely

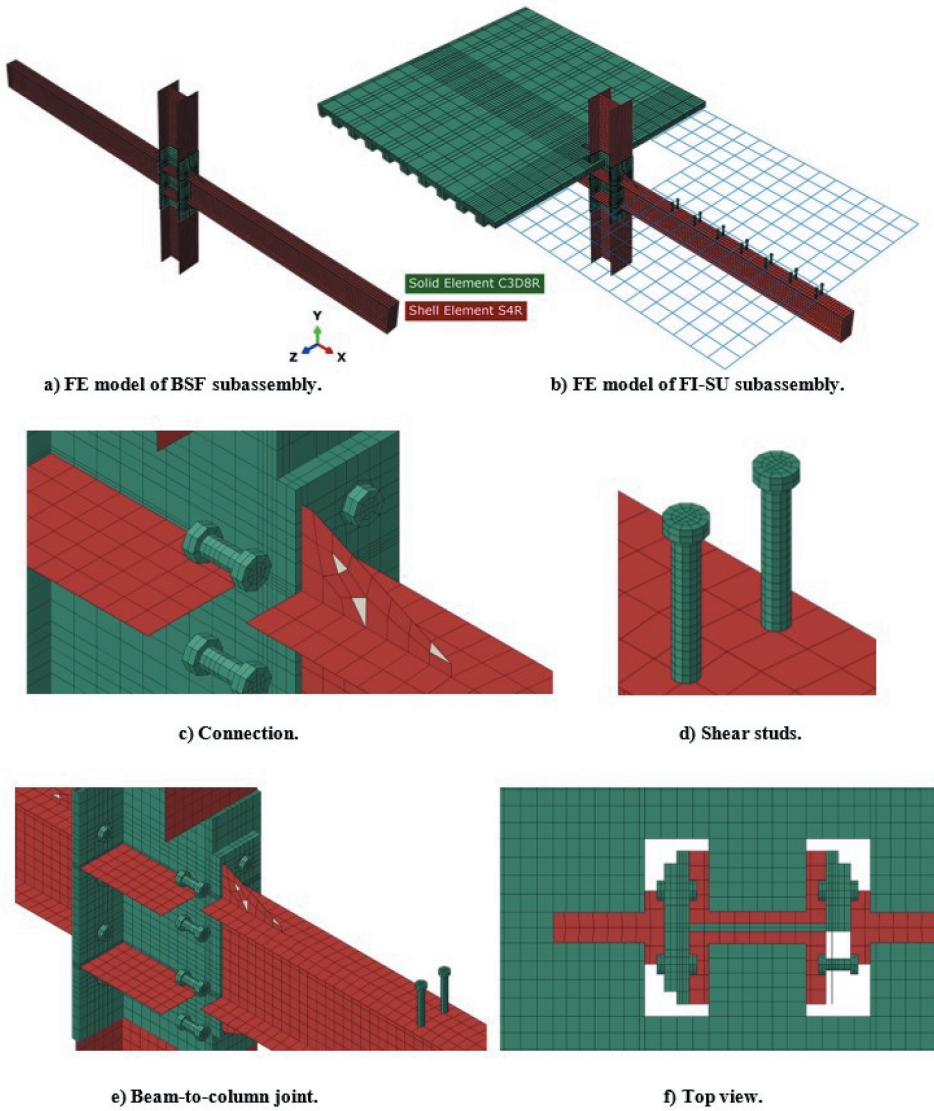


**Figure 8.** 3D FE models of two interior joint specimens.

the flange buckling and slab cracking, both features being showcased in Figs. 12 and 13. Therefore, the numerical model is reliable enough for attaining the objectives of this study.

## 5. Parametric Assessment

### 5.1. Model Description

After its benchmarking, the model was employed to study the effects of varying configurations of the RWS connection on the response to cyclic actions. The focus was made on i) the distance to the first perforation ( $S = 1.20 h, 1.00 h, 0.65 h$ , and  $0.50 h$  where  $h$  is the beam height), ii) the perforation diameter ( $d_0 = 0.80 h, 0.65 h$  and  $0.50 h$ ), and iii) the allocation of shear studs on the protected zone (either absent or present) leading to the provision of 9 to 7 stud rows over the whole length of the beam. The first case represents a high beam-slab coupling, while the second represents a low beam-



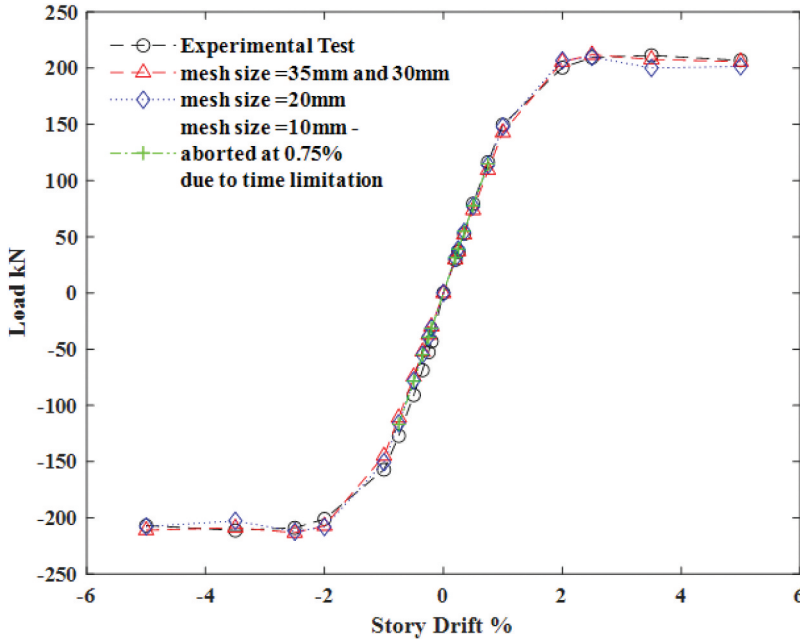


Figure 9. Load-Drift Skelton curves for FE models with different resolutions.

slab coupling. Further decoupling of the slab for the low and non-composite actions is achieved by providing a gap of 25 mm around the column perimeter for the cases where this was required, as shown in Fig. 14. A slab thickness of 150 mm corresponding to a Comflor 80 metal deck was considered for all models, as done in (Chaudhari 2017; Chaudhari et al. 2019).

The baseline model is comprised of compact European beam and column sections, which comply with code specifications stated in Eurocodes 3, 4 and 8. Rib stiffeners were avoided, while 6 mm doubler plates were provided to strengthen and stiffen the panel zone. Table 1 summarizes the properties of all structural elements allocated. The model was excited by a drift time history in accordance with the prequalification protocol defined in AISC 341 (2016) as shown in Fig. 15. The characteristics of all specimens and the naming convention for each one are presented in Table 2 and Fig. 16, respectively.

## 5.2. Nominal capacities of the protected zones

Nominal (code-specified) load-bearing capacities of the connection are expected to be governed by the full plastification of the reduced cross-section. For the case where joint slab-beam action is prevented, the nominal moment capacity is given by Eq. 1:

$$M_{pl,Rd,RWS} = f_y \left( W_{pl} - \frac{d_o^2 t_w}{4} \right) \quad (1)$$

Where  $M_{pl,Rd,RWS}$  is the plastic moment considering an idealized elastoplastic material model for steel,  $f_y$  is the yield stress,  $W_{pl}$  is the plastic modulus of the steel section,  $d_o$  is the perforation diameter, and  $t_w$  is the web thickness.

The nominal capacity of the composite section is calculated considering joint deformation of both the slab and the beam. Firstly, the steel deck is transformed into an equivalent uniform thickness slab by matching their cross-sectional areas. For this study, a 100 mm thick equivalent slab ( $t_{se}$ ) is found. This leads to a “virtual analysis gap” of 50 mm due to the difference among the equivalent thickness

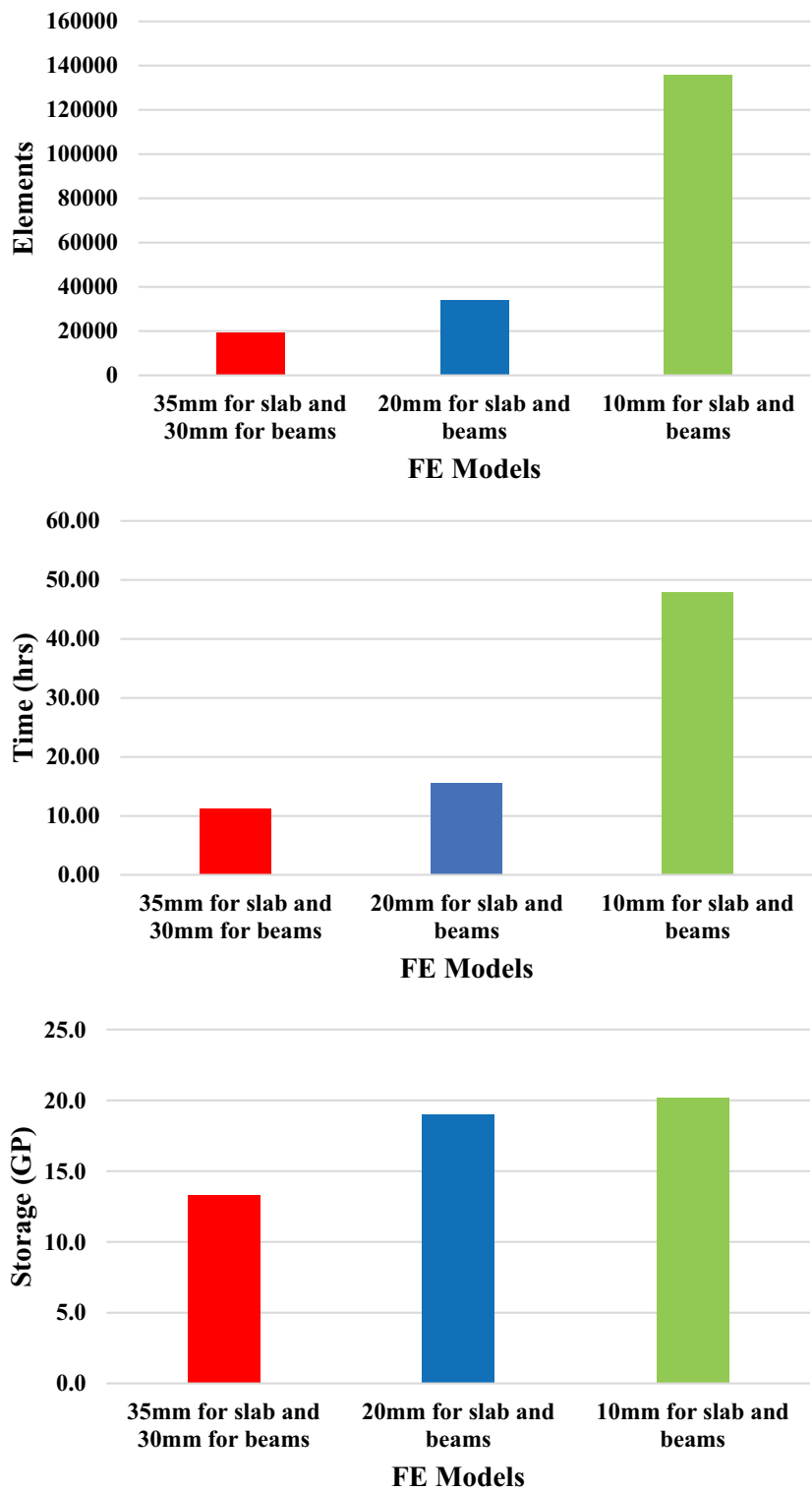


Figure 10. Performance of different mesh resolutions.



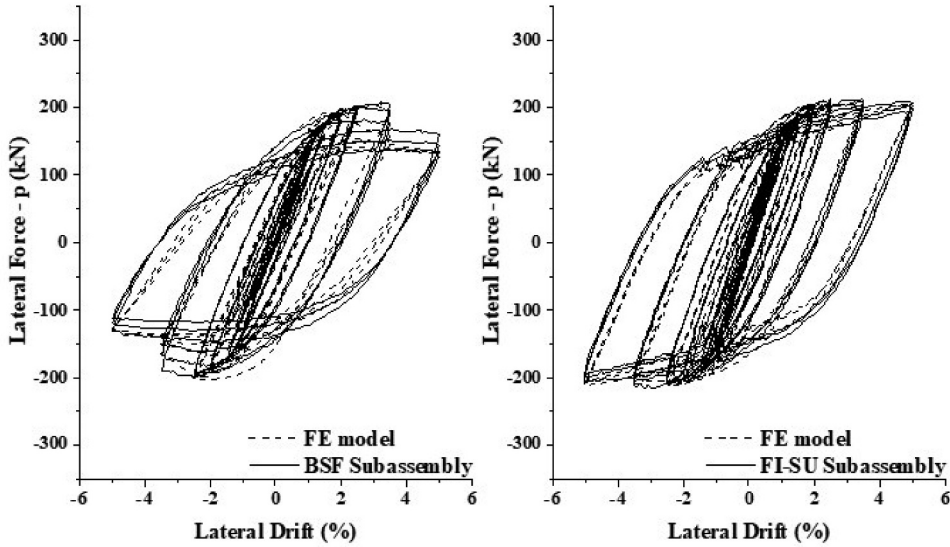


Figure 11. Benchmarking of the FEM Hysteresis cycles.

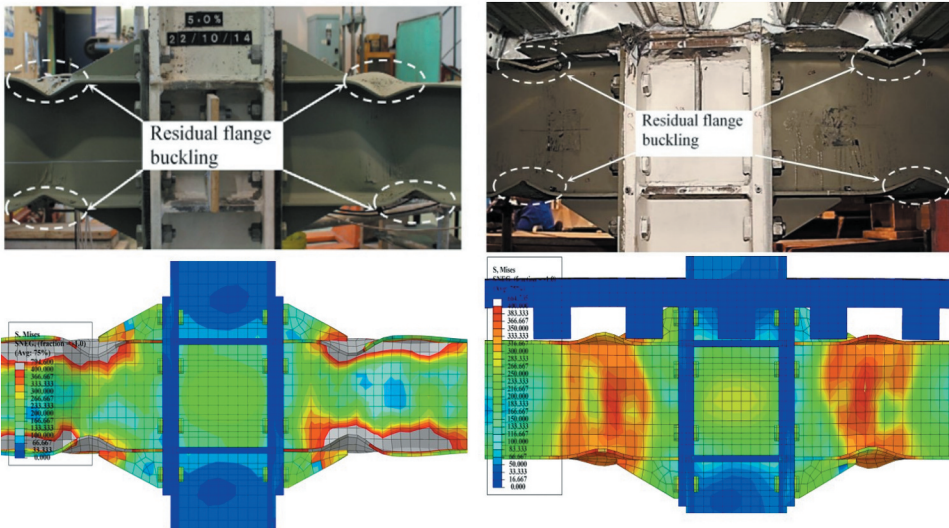
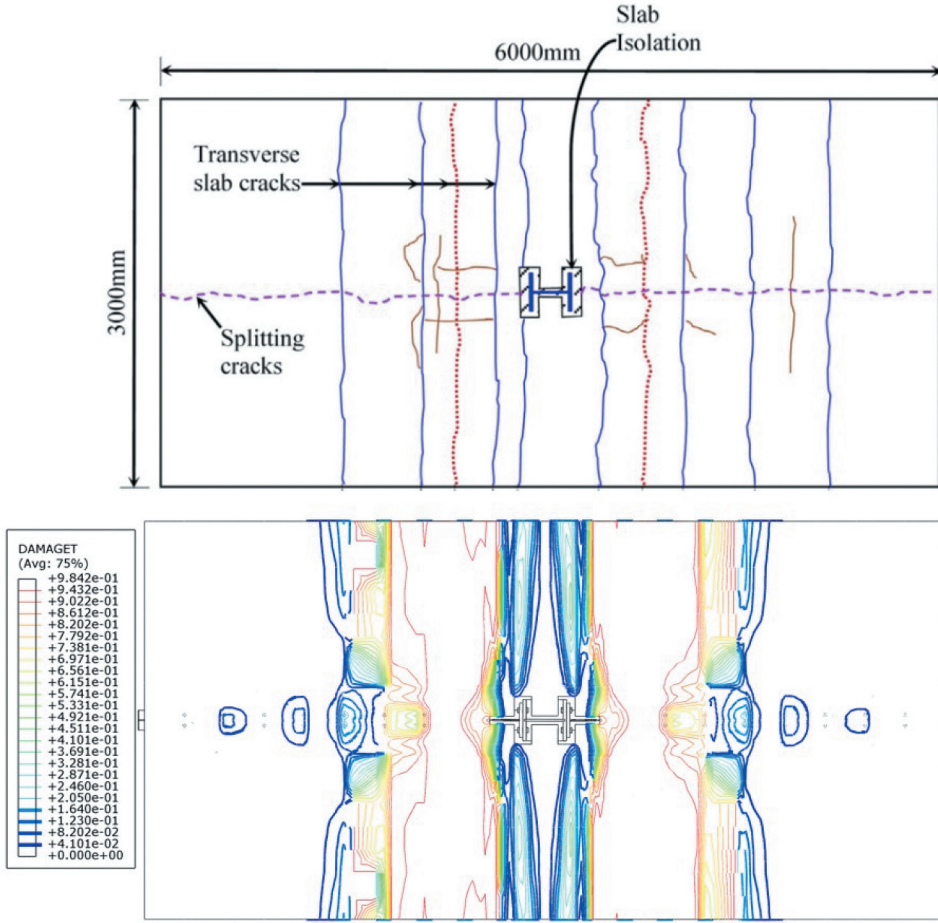


Figure 12. Comparison of local buckling between experimental tests (Chaudhari 2017; Chaudhari et al. 2019) and FE model (with render the thickness of the shell).

and the real thickness of the steel deck. Then, the effective width of the composite slab ( $b_e$ ) is calculated according to code specifications (Eurocode 2005c) finding that it is 8 times the equivalent slab thickness, namely, 800 mm. The comparable cross-section for assessing the nominal moment capacity is shown in Fig. 17.



**Figure 13.** Comparison of local buckling between experimental tests (Chaudhari 2017; Chaudhari et al. 2019) and FE model (with render the thickness of the shell).

Then, it is possible to consider Whitney's equivalent rectangular stress theory (Eurocode 2005c) to find the ultimate capacity of the ensemble. Firstly, peak compressive and tensile actions on both beam and slab must be calculated, following Eqs (2), and (3):

$$C = 0.85 f'_c b_e t_{se} \quad (2)$$

$$T = f_y (A_g - t_w d_o) \quad (3)$$

Where  $C$  is the compression force in the cross-section,  $f'_c$  is the nominal compression resistance of concrete in the slab,  $b_e$  is the thickness of the equivalent T section to account for shear lag in the slab,  $t_{se}$  is the slab thickness,  $T$  is the tension load on the cross-section, and  $A_g$  is the gross cross-section of the steel beam without perforations. In this case, the tension capacity of the beam at the reduced cross-section is lower than the compression action that can be sustained within the slab. Consequently, the neutral axis will be within it. The depth of the equivalent uniform stress field is given by:

$$a = \frac{T}{0.85 f'_c b_e} \quad (4)$$

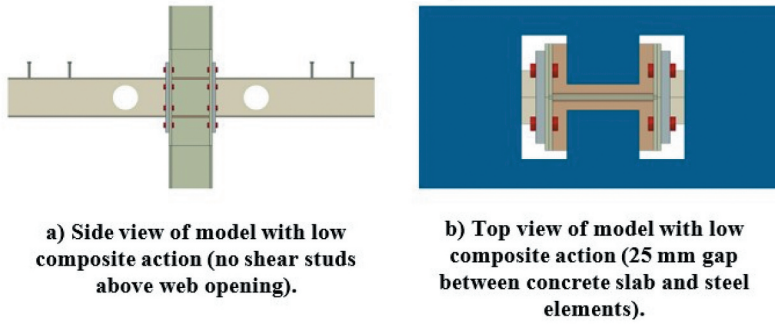


Figure 14. Model with low composite action.

Then the moment capacity of the cross-section can be computed by multiplying the tensile action by its lever arm on the cross-section, leading to the following expression for the nominal moment capacity ( $M_{pl,Rd}$ ):

$$M_{pl,Rd} = T \left( \frac{H}{2} + g + t_{se} - \frac{a}{2} \right) \quad (5)$$

Where  $H$  is the beam depth,  $g$  is the gap due to the difference between the real thickness of the steel deck and its equal-area idealization. For the hogging moment, the compression fibre is on the bottom, while the steel within the slab allows for an increase of the internal tensile action. However, only minimum reinforcement to prevent cracking due to shrinkage was provided, and consequently, its effect on capacity can be ignored. If that is the case, the hogging moment capacity will be the same as provided by the beam alone, in accordance with Eq. (1). A summary of the diverse nominal moment resistances is provided in Table 3.

### 5.3. FE Results

Lateral load and interstorey drift relationships are depicted in Figs. 18–20. For all cases, wide and stable hysteresis cycles without pinching are observed. Likewise, drifting away from the zero ordinate is at most slight, indicating that residual deformations are symmetrical, following the loading protocol. This indicates that buckling of end plates and yielding outside protected zones was mild, leading to symmetrical strain reversals.

The analysis was terminated when the specimen reached an interstorey drift of 6%; a loss of moment capacity larger than 20% of the maximum value was observed; the analysis failed to converge or there was a failure of any of the shear studs or bolts in the end plate. The great majority of RWS of specimens (84%) achieved the 6% threshold and all exceeded a 4% interstorey drift demand. The latter is the performance standard that a connection must satisfy if it is going to be used in special moment resisting frames, according to AISC-341 16 specifications (2016). The results are summarized in Table 4.

There is a significant difference among the yield drifts of beams highly coupled with the slab and specimens without shear studs. Median and 10–90%ile ranges for specimens with fully coupled beams and slabs are 1.50% and [1.31%, 1.57%] while for uncoupled beams they are 1.88 and [1.6, 1.98]. Furthermore, student's  $T$  pairwise tests have a  $p$ -value of  $1.94 \times 10^{-7}$ , indicating that the means of both groups are statistically different. Contrarily, the yield interstorey drift of specimens with low slab-beam coupling is similar to what is observed for the highly coupled case. A median value of 1.50% is observed, while the 10–90<sup>th</sup> percentile ranges in [1.29%, 1.79%], which hints at a larger variability. The means of both groups are not statistically different for a 95% confidence as the  $p$ -value associated with Student's  $t$ -test with paired samples is 0.125. It must be stressed that the computed yield drifts are an

**Table 1.** Dimensions and detailed configuration of the joint in the parametric study.

Element	Section type	Material
Beam	IPE300	S355
Slab	—	Concrete $f'_c = 30$ MPa, Rebar $f_y = 515$ MPa.
Column	HEB320	S355
Extended end-plate	530x260x25	S355
Bolt	M24	Class 10.9
Continuity plate	279x144.25x16	S355
Doubler plates	730x279x6	S355

The concrete slab, studs, and reinforcement steel rebars were kept the same as the experimental test (Chaudhari 2017; Chaudhari et al. 2019).

upper estimate. The flexural stiffness of steel cross sections is significantly affected by residual stresses caused by the cooling of the hot rolled element in the mill as both compressive and tensile yielding stresses can be introduced all over the cross-section. Their distribution pattern depends on the fabrication process and therefore their modelling would be specimen dependent. Thus, this made their inclusion in this study extremely cumbersome.

Table 5 showcases the observed moment capacity of the connection normalized by the bare section nominal moment capacity (without a slab). At most, it is observed that the peak moment resistance reaches 1.5 times the nominal capacity of the bare, reduced steel section. Contrarily, for all perforation sizes considered in this study, the moment capacity of the composite cross-section ranges between 1.9 and 2 times the capacity of the beam with perforations at the critical (smallest) cross section (Table 3). This is expected as full plastification of the reduced cross section solely in tension is unlikely to happen before the full development of the Vierendeel mechanism along the perforation edges. For that reason, it is more sensible to express the maximum moment capacity of the connection in terms of the plastification moment of the bare steel reduced section, according to Eq. (1), and presented in Table 5.

### 5.3.1. Effect of Perforation Diameter ( $d_o$ )

The results for connections with an opening equal to 80% of the beam's height indicate that the nominal capacity of the bare beam is reached if low composite action is present, as the peak moment ranges between 0.9 and 1.06 the nominal value, being 0.94 the average for the hogging moment and 1.00 for the sagging moment. This is expected as the slab provides an additional constraint to buckling and bending of the upper plastic hinges that make up the Vierendeel mechanism. Yet, as the ratio is close to one, it can be considered that both the Vierendeel Mechanism and the yielding of the critical cross-section are concurrent. When a high composite action is enforced, the moment capacity increases sizably, but it is not enough to reach what is expected for the composite section, which is close to double the plastification moment of the bare section alone with tension in the upper flange and compression at the bottom (Table 3). The average values for the ratio between the peak moment observed and the nominal capacity of the bare steel section are 1.09 and 1.36 for hogging and sagging moment capacity, while the minimum and maximum values are 0.94 and 1.48. As observed in the previous case, there is a significant difference between sagging and hogging moments, which is explained by the additional constraint on buckling offered by the slab. There is a slight reduction in capacity as the perforation is made closer to the column, but the data does not indicate a clear trend. Still, it is a good course of action to follow the SCI P355 guidelines (Lawson and Hicks 2011) in that regard; thus, allowing for a space of at least one perforation diameter from the column face to the centre of the perforation.

When the composite action is impeded in specimens with  $d_o = 0.8 h$  (i.e. non-composite), the peak moment reaches values that range between 0.86 and 0.83 of the nominal capacity, being similar for both sagging and hogging moments. Avoidance of shear transfer studs allows for relative slippage between the steel section and the slab; thus buckling is more likely to occur, making behaviour being controlled by the development of the Vierendeel mechanism along the opening edges. On the other

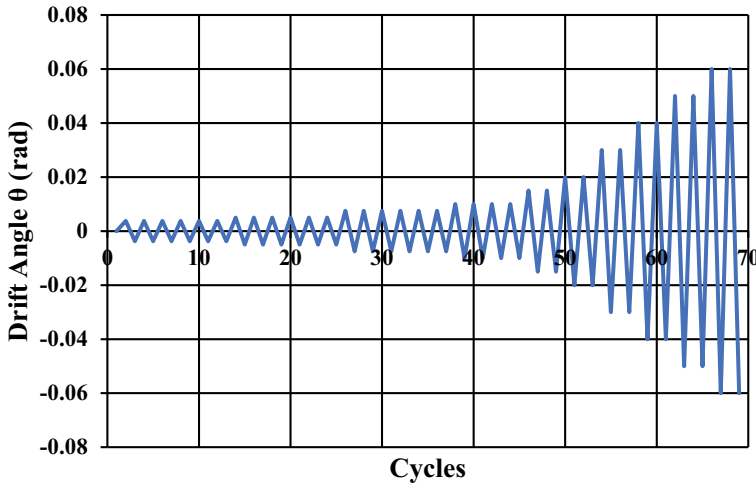


Figure 15. AISC 2016 loading protocol (2016).

hand, results indicate that there is a limited role of the spacing between the column face and the perforation.

All cases reached a story drift of 6%, except the specimen with high composite action with the first perforation allocated at a distance from the column equal to 1.2 times the height of the beam (R-C-H-80d-120S). As the analysis was terminated at this threshold, the ductility estimates are lower bound. Still, cases where there is low or high beam-slab interaction show interstorey drift ductility larger than 4, while for cases where the interaction was prevented, it ranges between 4 and 3 (Table 4).

Lower diameter perforations (0.65 h and 0.5 h) uncover the effect of overextending the distance between the column face and the centre of the perforation. For spacings,  $S = 1.2 h$  and  $1.0 h$ , the observed ultimate interstorey drift is less than 6%; yet, it is larger than 4.0% or close to this value (values of 3.96% were obtained for specimen R-C-H-50d-120S) indicating that even for these configurations, performance would allow for inclusion in special moment frames (ANSI/AISC 341-16 2016). Nevertheless, going beyond SCI-P355 (Lawson and Hicks 2011) recommendations is not advisable and can diminish deformation capacity significantly.

The ratio of peak moment capacity to nominal resistance reduces significantly as the opening size becomes smaller. For  $d_o = 0.65 h$  and beams with a high composite action; the average value is 1.22 for the sagging moment and 1.13 for the hogging moment, which is 10% less than was observed for the connection with  $d_o = 0.8 h$ , whilst the difference is marginal for the hogging moment. For  $d_o = 0.5 h$  with high composite action; averages for ratios of observed peak resistances and nominal values for the sagging and hogging moments are 1.18 and 1.15, respectively. Thus, for that case, capacity increases as a by-product of strengthening of  $T$ -stubs following the Vierendeel mechanism, rather than the true composite action. For  $d_o = 0.5 h$  and  $0.65 h$  specimens with low and no composite action, resistance ranges between 1.19 and 0.93 times the nominal capacity, observing comparable results for both sagging and hogging moments.

### 5.3.2. Strength Degradation

Moment capacity was checked at the end of the last load cycle. Table 4 shows strength degradation for all models. Remarkably, the great majority (84%) of RWS specimens reached an interstorey drift of 6% while being able to attain a moment larger than 80% of the maximum observed value. In all cases, the peak achieved moments in hysteresis cycles while the drift demand was less than 4% were larger than

**Table 2.** Summary of assessed specimens.

Model	Slab	Composite action	Web opening ( $d_o$ )	Web opening ( $S$ )	Comply with SCI P355
NR-NC	No	N/A	N/A	N/A	N/A
NR-C-H	Yes	High	N/A	N/A	N/A
NR-C-L	Yes	Low	N/A	N/A	N/A
R-C-H-50d-50S	Yes	High composite action	150	150	Yes
R-C-H-50d-65S	Yes		150	195	
R-C-H-50d-80S	Yes		150	240	
R-C-H-50d-100S	Yes		150	300	
R-C-H-50d-120S	Yes		150	360	
R-C-H-65d-50S	Yes		195	150	
R-C-H-65d-65S	Yes		195	195	
R-C-H-65d-80S	Yes		195	240	
R-C-H-65d-100S	Yes		195	300	
R-C-H-65d-120S	Yes		195	360	
R-C-H-80d-50S	Yes	Low composite action	240	150	No
R-C-H-80d-65S	Yes		240	195	
R-C-H-80d-80S	Yes		240	240	
R-C-H-80d-100S	Yes		240	300	
R-C-H-80d-120S	Yes		240	360	
R-C-L-50d-50S	Yes		150	150	
R-C-L-50d-65S	Yes		150	195	
R-C-L-50d-80S	Yes		150	240	
R-C-L-50d-100S	Yes		150	300	
R-C-L-50d-120S	Yes		150	360	
R-C-L-65d-50S	Yes	Non-composite models	195	150	No
R-C-L-65d-65S	Yes		195	195	
R-C-L-65d-80S	Yes		195	240	
R-C-L-65d-100S	Yes		195	300	
R-C-L-65d-120S	Yes		195	360	
R-C-L-80d-50S	Yes		240	150	
R-C-L-80d-65S	Yes		240	195	
R-C-L-80d-80S	Yes		240	240	
R-C-L-80d-100S	Yes		240	300	
R-C-L-80d-120S	Yes		240	360	
R-NC-50d-50S	No	Non-composite models	150	150	No
R-NC-50d-65S	No		150	195	
R-NC-50d-80S	No		150	240	
R-NC-50d-100S	No		150	300	
R-NC-50d-120S	No		150	360	
R-NC-65d-50S	No		195	150	
R-NC-65d-65S	No		195	195	
R-NC-65d-80S	No		195	240	
R-NC-65d-100S	No		195	300	
R-NC-65d-120S	No		195	360	
R-NC-80d-50S	No	Non-composite models	240	150	No
R-NC-80d-65S	No		240	195	
R-NC-80d-80S	No		240	240	
R-NC-80d-100S	No		240	300	
R-NC-80d-120S	No		240	360	

80% of the maximum, making all specimens compliant with the requirements for their deployment into special moment frames, according to AISC (2016).

All non-composite RWS and solid models (i.e. no slab) experienced a large strength degradation of up to 22.6% due to the absence of bracing, which makes them susceptible to lateral-torsional buckling. Whilst for connections with low-composite action, where a limited number of studs is provided even in the protected zone; but not enough for full shear transfer among slab and beam, strength loss is at most 10.9% and the average reaches 6.3%. For connections with the full composite action, even with studs within the protected zone, the average strength degradation reaches 3.2%, but the result is highly influenced by outliers where large openings are provided ( $d_o = 0.8h$ ). Clearly, the slab has a positive effect in controlling



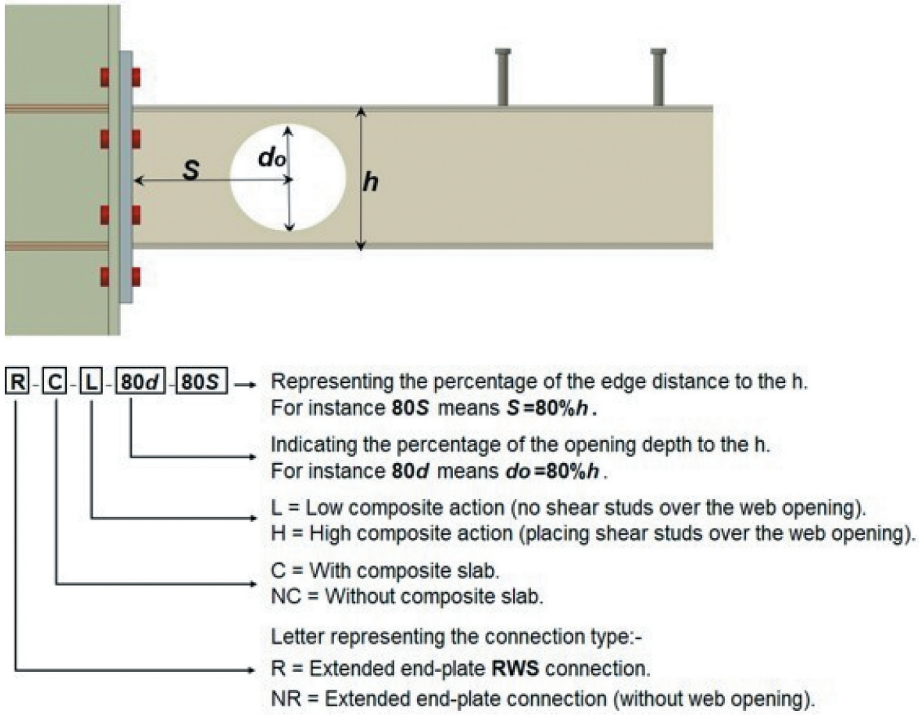


Figure 16. Model identifier.

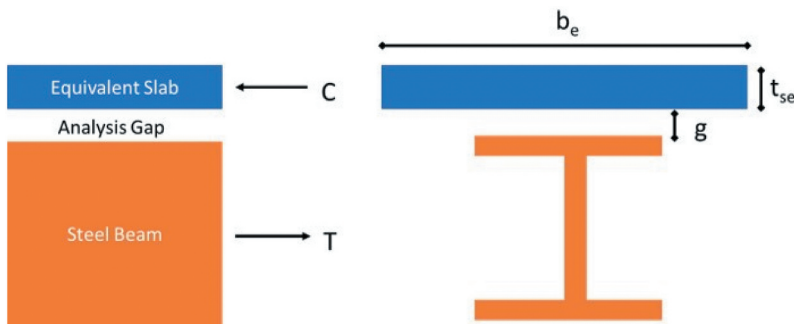


Figure 17. Equivalent composite section for nominal moment capacity assessment, sagging moment.

out-of-plane buckling of the reduced web section, making it highly unlikely if the perforation diameter is less or equal than 0.65 times the beam depth. For larger diameters, namely, 80% of the beam's depth, noticeable but limited, strength degradation is observed, reaching, at most 12.8%.

### 5.3.3. Failure Modes and Stress and Strain Distribution

As stated before, all specimens reached a 4% interstorey drift demand without significant loss of structural integrity, making them suitable for use in special moment frames. Moreover, most achieved

**Table 3.** Nominal moment capacities of main specimen typologies.

Specimen		Nominal Moment Resistance [kN-m]	
Description	ID	Sagging	Hogging
Non composite, $d_0 = 0.80h$	xx-NC-80d-xx	187	187
Non composite, $d_0 = 0.65h$	xx-NC-65d-xx	199	199
Non composite, $d_0 = 0.5h$	xx-NC-50d-xx	209	209
composite, $d_0 = 0.80h$	xx-C-80d-xx	360	187
composite, $d_0 = 0.65h$	xx-C-65d-xx	388	199
composite, $d_0 = 0.5h$	xx-C-50d-xx	416	209

a 6% interstorey drift without losing their load-bearing capacity. However, there are significant differences in how this performance was achieved, as outlined in Table 6.

In overall terms, the provision of perforations leads to a protected zone, where inelastic action can happen without global instability, as shown in Figs. 21–28. This is accomplished by yielding through the Vierendeel Mechanism and plastification of the reduced cross-section. The latter also induces buckling without tearing the bottom flange, due to strain reversals in tension and compression. These mechanisms preserve the gravitational load-bearing capacity of the connection, thereby allowing for extensive deformation capacity.

Although inelastic action is prevented on the column, bending of bolts and buckling of end plates are observed. These undesired, potentially fragile phenomena occur in RWS specimens with low composite action and with a perforation diameter of 0.5 times the beam height only (Figs. 21 and 22). For RWS specimens where shear studs are provided in the protected zone, they occur in almost all cases. For specimens with a perforation diameter equal  $0.8h$ , the formation of the Vierendeel mechanism is inevitable (Figs. 25 and 26). Also, it developed in those specimens with a perforation diameter equal  $0.65h$  having low composite action (Figs. 23 and 24).

However, it must be stressed that these undesired failure modes occur for a large interstorey drift demand, in excess of 4% and could be potentially limited if capacity design principles are applied considering the specific features of RWS connections, as detailing is done in accord with testing for non-RWS specimens. Possible strategies are: designing end plates to consider the effective plastification capacity of the composite section, whilst accounting for steel strain hardening, and elimination of shear studs above the plastic zone, to allow for the formation of Vierendeel mechanism, alike connections without slabs. It must be stressed that out-of-plane instability and tearing of structural elements, either beams, columns, or joints was avoided.

#### 5.3.4. Damage Patterns on the Slab

Figures 29 and 30 depict different patterns of slab damage in both tension and compression, for models where there is high and low composite actions. Clearly, there is extensive cracking in tension for all cases, indicating that reducing the number of shear studs may allow for some relative slippage, as hinted by the cap on moment resistance, but joint deformation is still important, leading to adverse transfer of shear strain into the concrete slab.

Contrarily, compressive crushing shows a more varied behaviour depending on the degree of coupling of the beam and the slab. For low composite action, damage is limited, particularly when the opening diameter is  $0.65h$  or larger. Rather, it happens due to stress concentration in the vicinity of the web opening. For high composite action, damage is more widespread, indicating that the slab plays a critical role by supporting compressive stresses. Among specimens with high composite action,



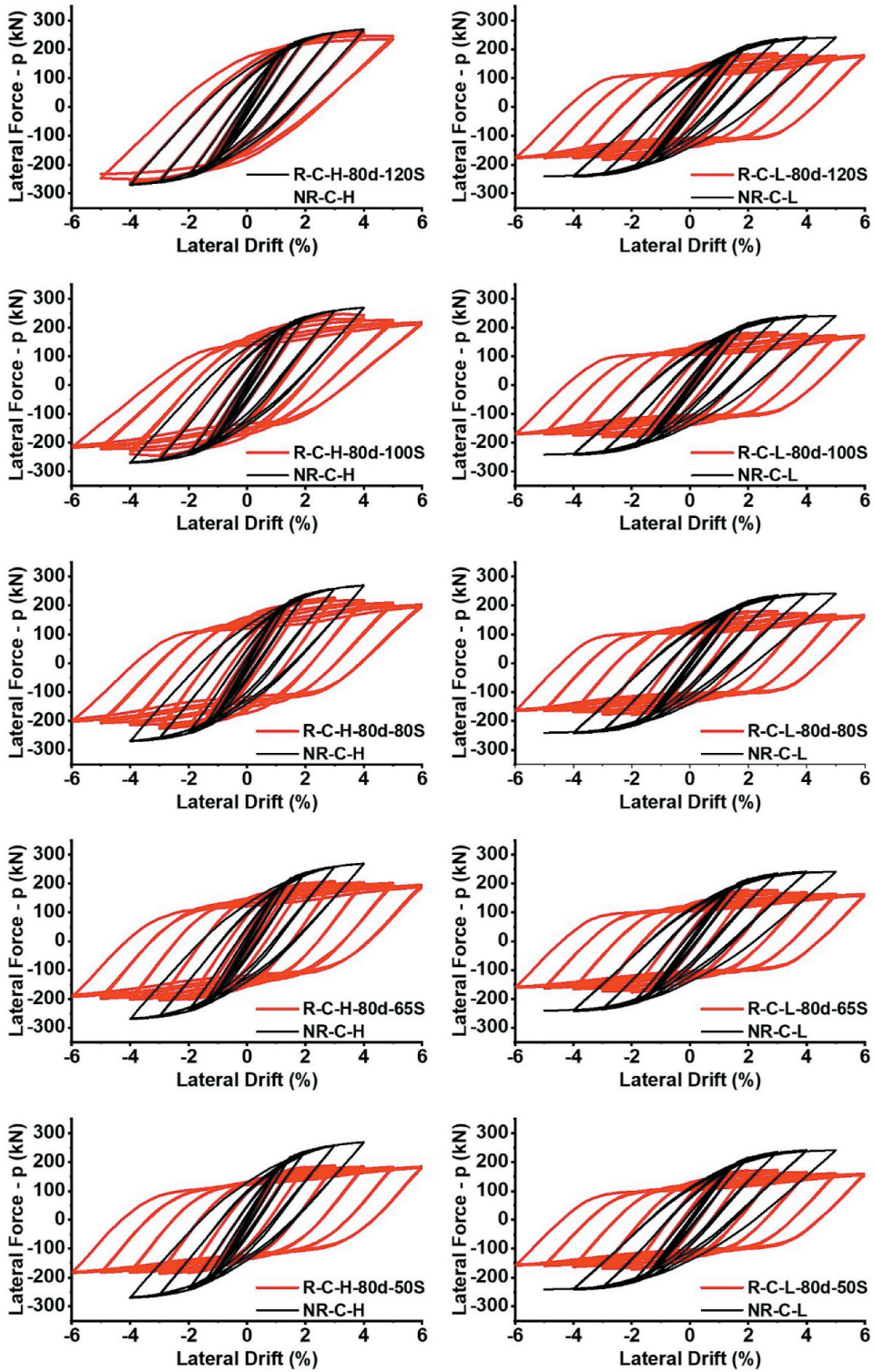


Figure 18. Hysteretic curves of solid model and models with the diameter of the opening equal to 0.8 h.

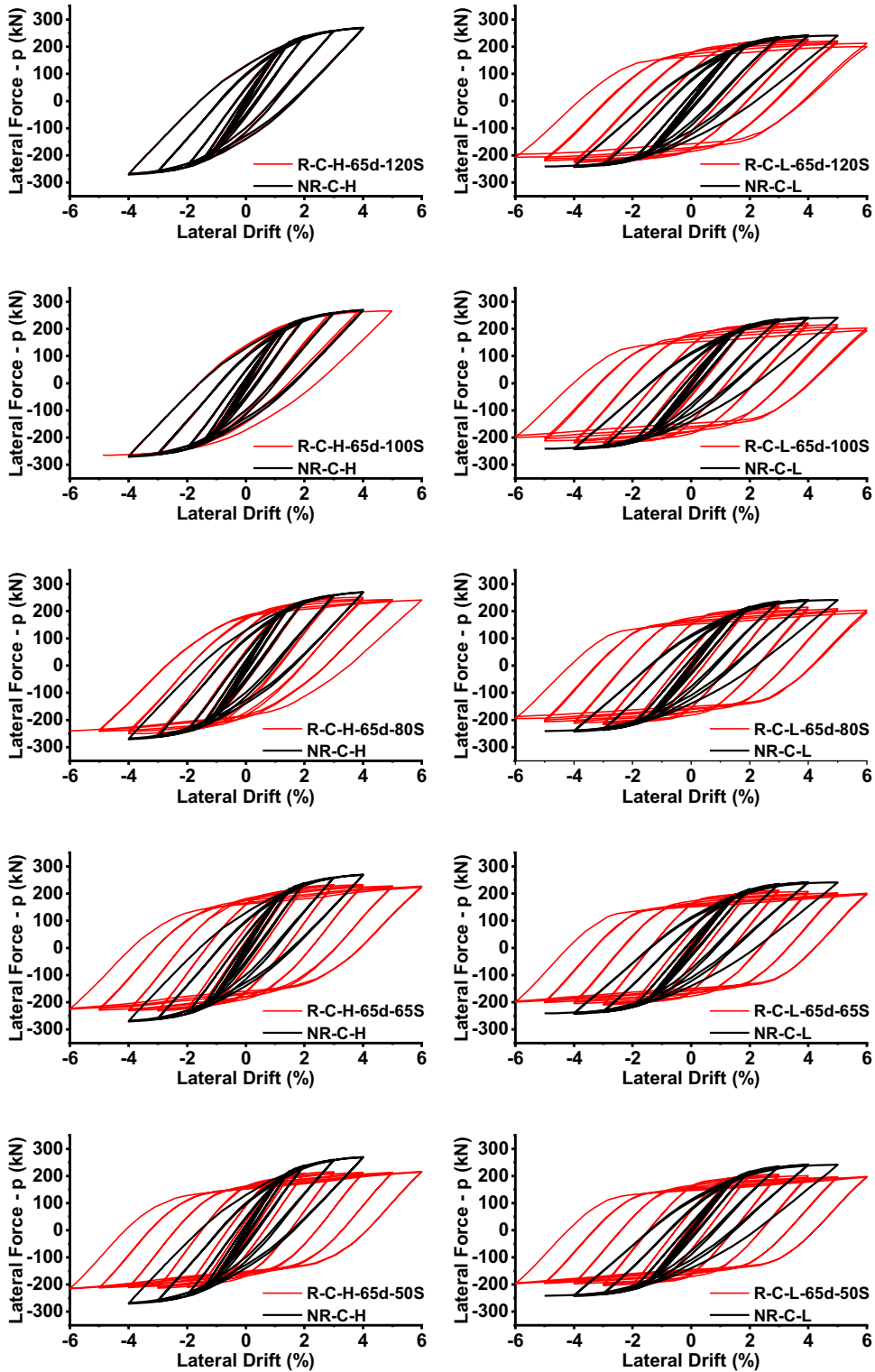


Figure 19. Hysteretic curves of solid model and models with the diameter of the opening equal to 0.65 h.

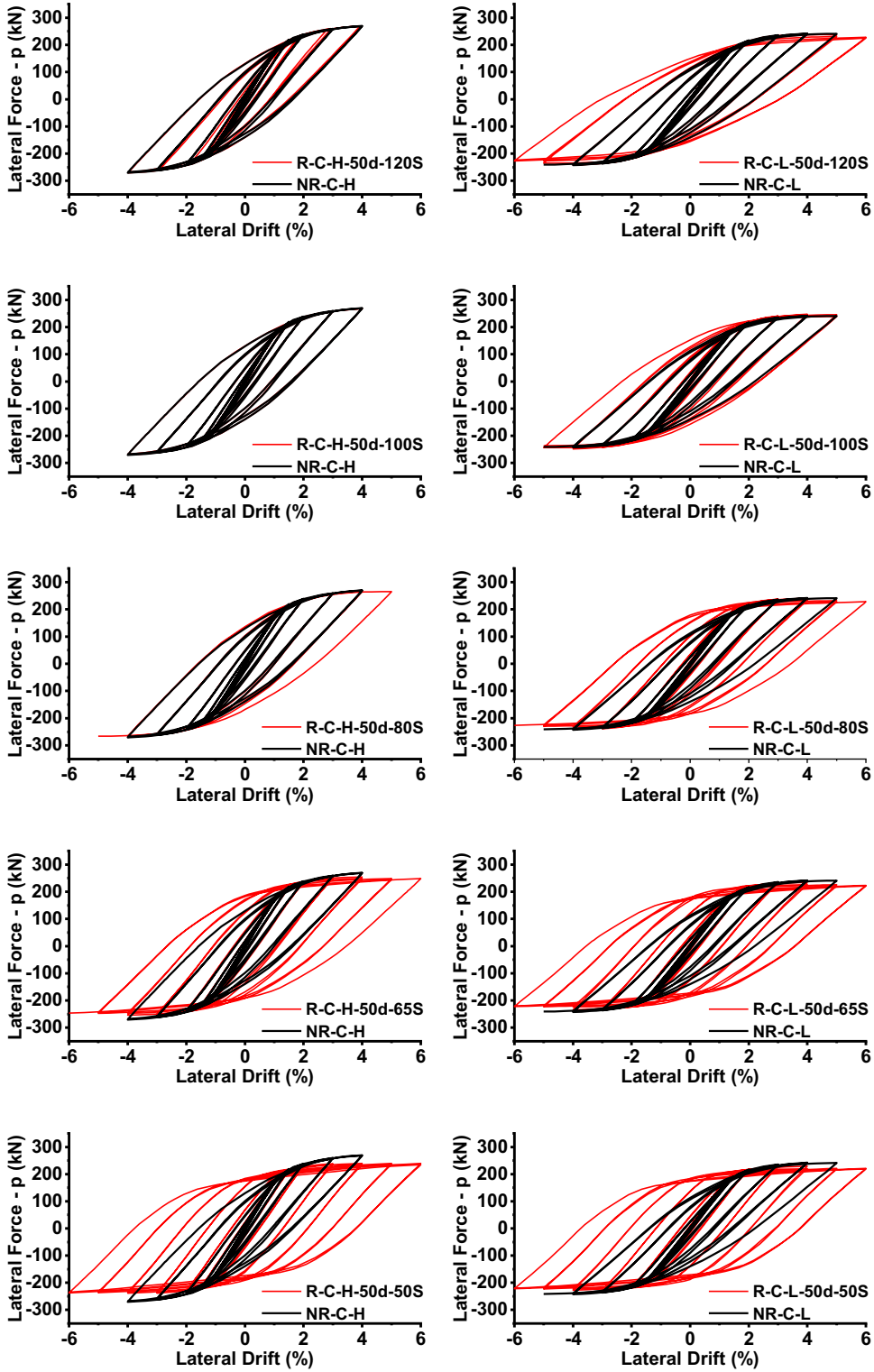


Figure 20. Hysteretic curves of solid model and models with the diameter of the opening equal to 0.5 h.

**Table 4.** Interstory drift deformation capacity and strength degradation of all specimens.

Models	Lateral Load (kN)		Yield Interstory Drift $\theta_y$ (%rad)		Ultimate Interstory Drift $\theta_u$ (%rad)		Interstory Drift Ductility		Dissipated energy (kN.m)	Strength degradation (%)	
	+ve	-ve	+ve	-ve	+ve	-ve	+ve	-ve		+ve	-ve
NR-C-L	242.0	242.4	1.79	1.79	5.00	5.00	2.79	2.79	15.27	0.4	0.6
NR-C-H	269.5	270.3	1.59	1.59	4.00	4.00	2.52	2.52	13.95	0.0	0.0
NR-NC	232.1	230.1	2.14	2.14	6.00	6.00	2.80	2.80	27.26	16.4	15.6
R-C-L-80d-120S	185.6	183.6	1.39	1.39	6.00	6.00	4.32	4.32	23.26	3.6	3.2
R-C-L-80d-100S	183.7	181.1	1.35	1.35	6.00	6.00	4.44	4.44	23.00	6.2	5.6
R-C-L-80d-80S	180.0	179.2	1.25	1.25	6.00	6.00	4.80	4.80	23.22	7.9	8.3
R-C-L-80d-65S	178.1	177.2	1.24	1.24	6.00	6.00	4.84	4.84	22.74	8.8	9.1
R-C-L-80d-50S	172.4	171.9	1.35	1.35	6.00	6.00	4.44	4.44	22.25	7.4	8.1
R-C-H-80d-120S	260.8	264.6	1.63	1.65	5.00	5.00	3.07	3.03	21.55	5.8	6.4
R-C-H-80d-100S	247.6	249.4	1.50	1.50	6.00	6.00	4.00	4.00	27.86	11.8	12.8
R-C-H-80d-80S	227.4	226.0	1.39	1.39	6.00	6.00	4.32	4.32	28.15	10.6	10.9
R-C-H-80d-65S	207.7	204.6	1.33	1.31	6.00	6.00	4.51	4.58	27.73	5.9	5.8
R-C-H-80d-50S	188.2	185.8	1.21	1.21	6.00	6.00	4.96	4.96	23.50	2.0	1.1
R-NC-80d-120S	182.0	180.3	1.65	1.65	6.00	6.00	3.64	3.64	23.54	21.3	21.3
R-NC-80d-100S	178.5	177.3	1.65	1.64	6.00	6.00	3.64	3.66	23.49	20.1	20.4
R-NC-80d-80S	173.6	173.4	1.60	1.60	6.00	6.00	3.75	3.75	23.30	19.8	20.7
R-NC-80d-65S	175.4	175.1	1.60	1.60	6.00	6.00	3.75	3.75	22.73	21.4	22.2
R-NC-80d-50S	169.7	169.0	1.55	1.55	6.00	6.00	3.87	3.87	20.96	22.2	22.6
R-C-L-65d-120S	227.7	226.4	1.75	1.75	6.00	6.00	3.43	3.43	30.21	6.8	8.8
R-C-L-65d-100S	224.8	223.5	1.60	1.60	6.00	6.00	3.75	3.75	30.73	9.8	10.9
R-C-L-65d-80S	218.1	216.3	1.50	1.50	6.00	6.00	4.00	4.00	30.61	7.1	10.0
R-C-L-65d-65S	212.3	209.8	1.50	1.45	6.00	6.00	4.00	4.14	27.64	5.5	5.0
R-C-L-65d-50S	206.5	203.9	1.40	1.40	6.00	6.00	4.29	4.29	26.81	4.4	3.6
R-C-H-65d-120S	268.5	269.2	1.51	1.51	4.00	4.00	2.65	2.65	14.00	0.0	0.0
R-C-H-65d-100S	266.1	268.0	1.51	1.51	4.98	4.88	3.30	3.23	13.92	0.2	1.5
R-C-H-65d-80S	250.2	251.0	1.50	1.50	6.00	6.00	4.00	4.00	27.20	3.8	4.5
R-C-H-65d-65S	232.9	231.8	1.38	1.38	6.00	6.00	4.35	4.35	30.66	2.7	2.7
R-C-H-65d-50S	216.0	215.7	1.29	1.29	6.00	6.00	4.65	4.65	26.97	0.0	0.0
R-NC-65d-120S	217.3	214.9	1.95	1.90	6.00	6.00	3.08	3.16	28.34	16.7	21.1
R-NC-65d-100S	211.4	210.7	1.90	1.89	6.00	6.00	3.16	3.17	28.54	14.4	14.8
R-NC-65d-80S	208.7	208.4	1.88	1.88	6.00	6.00	3.19	3.19	28.71	19.3	19.3
R-NC-65d-65S	204.8	204.4	1.75	1.80	6.00	6.00	3.43	3.33	28.87	15.9	16.8
R-NC-65d-50S	201.7	201.4	1.80	1.80	6.00	6.00	3.33	3.33	28.10	20.0	19.4
R-C-L-50d-120S	241.7	242.1	1.80	1.80	6.00	6.00	3.33	3.33	24.38	5.7	6.3
R-C-L-50d-100S	247.5	248.4	1.69	1.69	5.00	5.00	2.96	2.96	17.73	4.2	5.2
R-C-L-50d-80S	240.6	238.9	1.68	1.69	6.00	6.00	3.57	3.55	25.46	5.4	5.5
R-C-L-50d-65S	234.1	234.3	1.61	1.61	6.00	6.00	3.73	3.73	28.83	4.6	5.0
R-C-L-50d-50S	229.0	228.1	1.60	1.60	6.00	6.00	3.75	3.75	29.72	3.6	2.6
R-C-H-50d-120S	269.6	270.9	1.58	1.58	3.96	3.98	2.51	2.52	13.92	0.0	0.0
R-C-H-50d-100S	268.8	269.9	1.55	1.55	4.00	4.00	2.58	2.58	14.03	0.0	0.0
R-C-H-50d-80S	267.0	268.8	1.53	1.53	5.00	5.00	3.27	3.27	14.72	0.7	1.0
R-C-H-50d-65S	254.6	253.7	1.45	1.45	6.00	6.00	4.14	4.14	27.16	2.6	2.8
R-C-H-50d-50S	239.9	238.3	1.40	1.40	6.00	6.00	4.29	4.29	28.20	0.3	0.3
R-NC-50d-120S	229.4	226.7	2.00	2.00	6.00	6.00	3.00	3.00	27.59	15.0	14.6
R-NC-50d-100S	225.7	224.0	1.98	1.98	6.00	6.00	3.03	3.03	27.69	16.0	15.4
R-NC-50d-80S	223.9	222.7	1.98	1.98	6.00	6.00	3.03	3.03	27.95	16.9	15.1
R-NC-50d-65S	221.9	221.2	1.97	1.97	6.00	6.00	3.05	3.05	27.86	16.5	15.5
R-NC-50d-50S	220.9	220.5	1.95	1.95	6.00	6.00	3.08	3.08	28.14	14.4	14.5

+ve and -ve refer to the direction of the applied load. +ve is when the actuator pushes to the right, while -ve is when it pulls to the left.

damage is lowest when the opening is 0.80 times the beam depth. Yet, this case displayed the largest structural efficiency, as the average peak moment reached 1.38 times the nominal capacity of the connection with the bare beam. This is explained by the fact that reducing the cross-section of the beam to the greatest extent, limits excess tensile actions within it; therefore, balancing compressive actions are lower, and induced damage is consequently milder. It seems that the best efficiency is

**Table 5.** Estimated and attained moment capacities for right beam.

Models	$M_{pl,Rd}$ or $M_{pl,Rd,RWS}$ kNm	Ratio of $M_{j,Rd}$ to steel beam	Normalized max $\frac{M_f}{M_{pl,Rd}}$		Normalized max $\frac{M_o}{M_{pl,Rd,RWS}}$	
			(sag)	(hog)	(sag)	(hog)
NR-C-L	223.1	0.966	1.14	−1.05	N/A	N/A
NR-C-H			1.19	−1.22	N/A	N/A
NR-NC			1.03	−1.02	N/A	N/A
R-C-L-80d-120S		1.154	1.01	−0.86	1.06	−0.90
R-C-L-80d-100S			0.96	−0.86	1.03	−0.92
R-C-L-80d-80S			0.88	−0.88	0.97	−0.96
R-C-L-80d-65S			0.86	−0.86	0.96	−0.96
R-C-L-80d-50S			0.89	−0.83	1.01	−0.94
R-C-H-80d-120S			1.34	−1.20	1.40	−1.25
R-C-H-80d-100S			1.38	−1.12	1.48	−1.20
R-C-H-80d-80S			1.30	−0.97	1.42	−1.06
R-C-H-80d-65S			1.17	−0.90	1.31	−1.00
R-C-H-80d-50S			1.03	−0.83	1.17	−0.94
R-NC-80d-120S	199.1	1.083	0.80	−0.80	0.84	−0.83
R-NC-80d-100S			0.79	−0.78	0.84	−0.84
R-NC-80d-80S			0.77	−0.77	0.84	−0.84
R-NC-80d-65S			0.78	−0.77	0.86	−0.86
R-NC-80d-50S			0.75	−0.75	0.85	−0.85
R-C-L-65d-120S			1.10	−1.01	1.08	−0.99
R-C-L-65d-100S			1.06	−1.02	1.06	−1.02
R-C-L-65d-80S			1.05	−0.99	1.08	−1.01
R-C-L-65d-65S			1.00	−0.95	1.05	−1.00
R-C-L-65d-50S			1.01	−0.91	1.07	−0.97
R-C-H-65d-120S	208.9	1.032	1.15	−1.22	1.13	−1.20
R-C-H-65d-100S			1.22	−1.21	1.22	−1.21
R-C-H-65d-80S			1.29	−1.14	1.32	−1.17
R-C-H-65d-65S			1.20	−1.04	1.26	−1.08
R-C-H-65d-50S			1.11	−0.95	1.17	−1.01
R-NC-65d-120S			0.96	−0.95	0.94	−0.93
R-NC-65d-100S			0.94	−0.93	0.94	−0.93
R-NC-65d-80S			0.92	−0.92	0.95	−0.94
R-NC-65d-65S			0.91	−0.90	0.95	−0.94
R-NC-65d-50S			0.89	−0.89	0.95	−0.94
R-C-L-50d-120S	208.9	1.032	1.23	−1.05	1.15	−0.98
R-C-L-50d-100S			1.21	−1.08	1.16	−1.03
R-C-L-50d-80S			1.21	−1.05	1.18	−1.03
R-C-L-50d-65S			1.20	−1.03	1.19	−1.03
R-C-L-50d-50S			1.18	−1.01	1.19	−1.03
R-C-H-50d-120S			1.16	−1.23	1.08	−1.15
R-C-H-50d-100S			1.17	−1.22	1.12	−1.17
R-C-H-50d-80S			1.25	−1.22	1.22	−1.19
R-C-H-50d-65S			1.28	−1.15	1.27	−1.15
R-C-H-50d-50S			1.20	−1.08	1.21	−1.10
R-NC-50d-120S	208.9	1.032	1.01	−1.00	0.95	−0.93
R-NC-50d-100S			1.00	−0.99	0.95	−0.94
R-NC-50d-80S			0.99	−0.99	0.97	−0.96
R-NC-50d-65S			0.98	−0.98	0.98	−0.97
R-NC-50d-50S			0.98	−0.97	0.99	−0.99

$M_{pl,Rd}$  = nominal plastic bending capacity for steel section;  $M_{pl,Rd,RWS}$  = nominal plastic bending capacity for steel section with web opening based on Eq. (1);  $M_{j,Rd} = 215.6$  kNm, the design resistance of the joint according to EC3 (Eurocode 2005b) (based on  $M_{pl,Rd}$  for solid beam and  $M_{pl,Rd,RWS}$  for the beam with opening);  $M_f$  = maximum beam moment at column face;  $M_o$  = maximum beam moment at the centre of RWS.

achieved by providing large openings and allowing for mild crushing and cracking of the concrete slab, which in turn provides a supplementary energy dissipation, which happens alongside with attainment of early plastic deformations around the web openings (Vierendeel mechanism). This approach can be applied to RWS connections with low and high composite action.

**Table 6.** FE results of the contribution of composite action for right beam and failure modes.

Model	Composite action	Number of shear studs' rows	Contribution of composite action		Failure modes
			(+ ve)	(– ve)	
NR-C-H	High	9	15.8%	20.5%	BF & BE
NR-C-L	Low	7	10.6%	3.5%	BF & BE
R-C-H-80d-120S	High composite action	9	66.6%	50.8%	VM, BF, & BE
R-C-H-80d-100S			74.9%	43.0%	VM, BF, & BE
R-C-H-80d-80S			69.3%	26.1%	VM
R-C-H-80d-65S			51.5%	16.7%	VM
R-C-H-80d-50S			37.6%	10.9%	VM
R-C-H-65d-120S			19.9%	28.9%	BF, FB, & BE
R-C-H-65d-100S			30.5%	29.9%	BF, FB, WB & BE
R-C-H-65d-80S			39.8%	24.3%	BF, WB & BE
R-C-H-65d-65S			32.9%	14.7%	FB, & WB
R-C-H-65d-50S			24.1%	6.9%	FB, & WB
R-C-H-50d-120S			13.9%	23.3%	BF, FB, & BE
R-C-H-50d-100S			17.3%	23.7%	BF, FB, & BE
R-C-H-50d-80S			25.8%	23.8%	BF, FB, & BE
R-C-H-50d-65S			29.9%	18.0%	BF, FB, WB & BE
R-C-H-50d-50S			22.7%	11.1%	FB, WB & BE
R-C-L-80d-120S	Low composite action	7	25.8%	8.2%	VM
R-C-L-80d-100S			21.9%	9.7%	VM
R-C-L-80d-80S			15.1%	14.4%	VM
R-C-L-80d-65S			11.6%	11.1%	VM
R-C-L-80d-50S		8	18.6%	11.2%	VM
R-C-L-65d-120S			14.5%	6.8%	VM & WB
R-C-L-65d-100S			13.5%	9.8%	VM & WB
R-C-L-65d-80S			14.1%	7.3%	VM & WB
R-C-L-65d-65S			10.8%	5.7%	VM
R-C-L-65d-50S		7	13.3%	2.7%	VM
R-C-L-50d-120S			21.2%	5.3%	BF, FB, & BE
R-C-L-50d-100S			21.1%	8.9%	BF, FB, & BE
R-C-L-50d-80S			22.2%	6.7%	BF, FB, & BE
R-C-L-50d-65S			21.6%	5.5%	VM, FB, & BE
R-C-L-50d-50S		8	20.4%	4.1%	VM, FB, & BE

BF = bolt bending (exceeded its capacity); BE = bending of extended end-plate; FB = flange buckling; WB = web buckling; and VM = Vierendeel mechanism. +ve and -ve refer to positive and negative moments of the right beam, respectively.

### 5.3.5. Contribution of Composite Action

The contribution of the low and high composite action to the overall strength capacity is shown in Table 6. The average contribution values for specimens with a low composite action are 17% and 7.8%, for sagging and hogging moments, respectively. While for those with high composite action, the average values are 37% and 23.5% for sagging and hogging moments, respectively. This hints that composite action keeps contributing to the overall moment capacity even if the reinforced concrete slab is extensively cracked and crushed. Thus, it could lead to the strengthening rather than weakening of the connection, if it is not properly accounted for. Thus, understanding the composite action effect on the seismic performance of the connections is very important for accounting for overstrength in both erection of new buildings and seismic retrofit.

The RWS models with low composite action have a low contribution of composite action to the overall strength capacity, ranging between 2.7% and 25.8% (Table 6). This eases the prediction of their moment strength capacity, which would be based on the plastic bending capacity of the connection furnished with a bare steel beam. For RWS models with high composite action, the contribution of composite action to the overall strength capacity ranged between 6.9% and 74.9%, noticeably higher. Consequently, ignoring slab effects in the design of RWS models where high composite action is allowed, can lead to unsafe design.

Interestingly, cracking and crushing of concrete were observed to be lower for a perforation size of  $0.8h$  compared to what was registered for perforation sizes equal to  $0.65h$  and  $0.5h$  (Fig. 29). Albeit



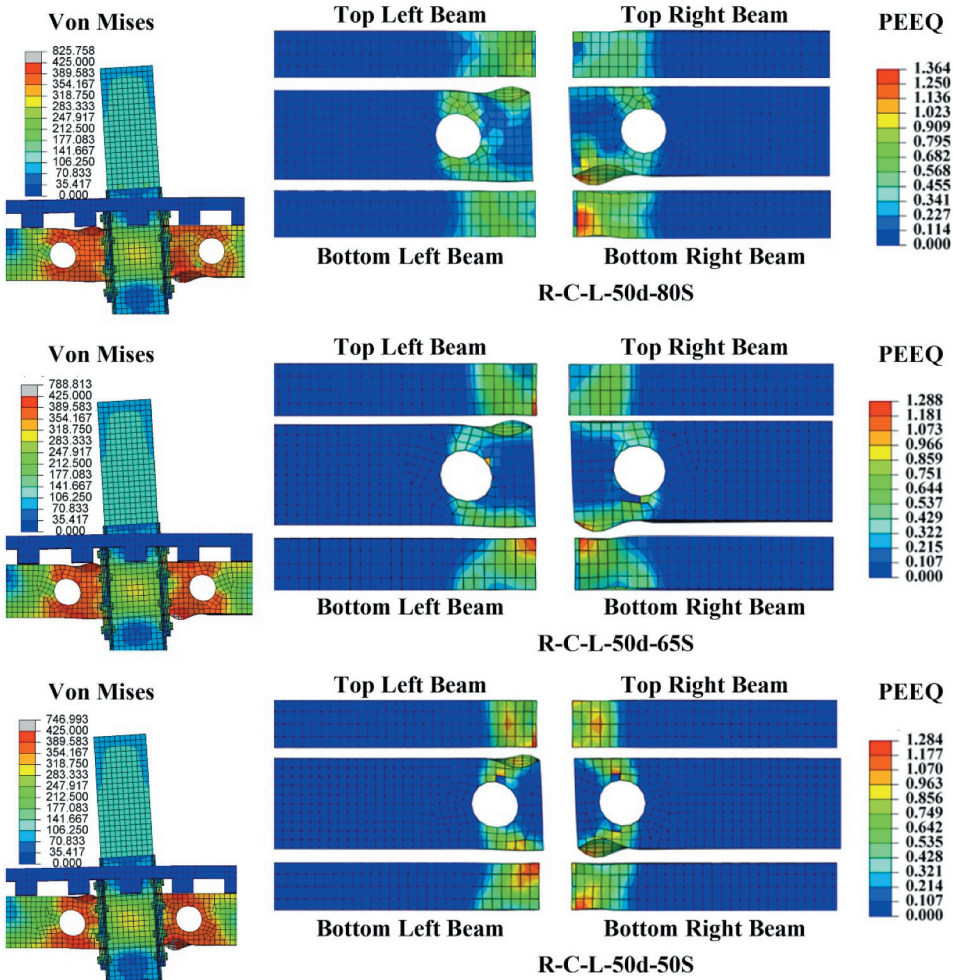


**Figure 21.** PEEQ and Von Mises stress distribution of RWS models with  $d = 0.5 h$  in the absence of shear studs over the protected zone.

explicit consideration of the slab in design may lead to a slight reduction of damage within it, the main reason for doing it is to preserve the strong column-weak beam design paradigm.

## 6. Discussion

The results indicate that composite RWS connections offer a large deformation capacity, of 4% interstorey drift, while keeping a moment capacity of at least 80% of the peak value, without inducing damage to columns and joints. Particularly, tearing of structural elements is prevented, being the most relevant non-ductile phenomena failure of bolts in the beam-column connection and shear transfer studs between the slab and the beam.

It was found that achieving the nominal resistance of the composite section is unlikely. Whilst for the specimens assessed in this study, this is close to two times the nominal capacity of the bare steel section, results indicate that the overall peak resistance under cyclic actions reaches 1.4 times the nominal capacity of the section (Table 5  $\frac{M_f}{M_{pl,Rd}}$ ). This was observed when shear transfer studs were placed in the protected zone (i.e. high composite action). This large divergence can be explained by the

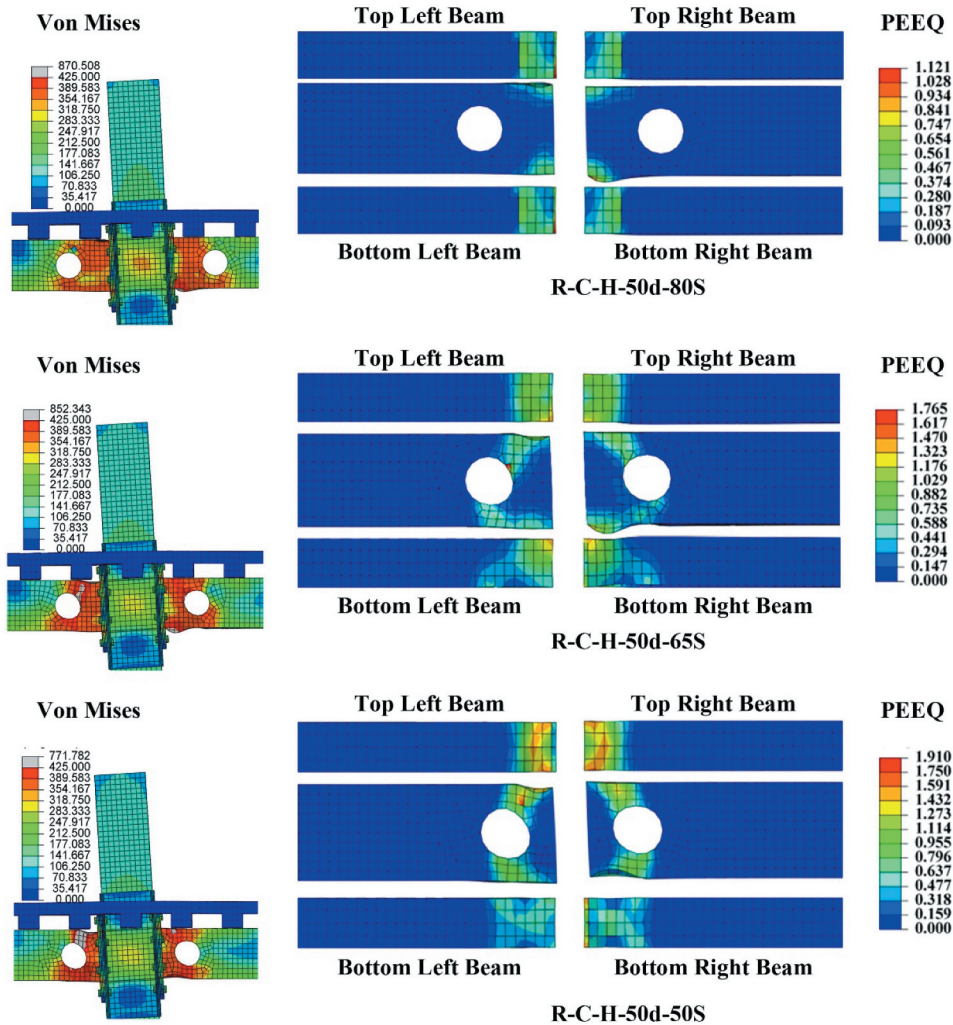


**Figure 22.** PEEQ and Von Mises stress distribution of RWS models with  $d = 0.5 h$  in the presence of shear studs over the protected zone.

characteristics of the reversible deformation demand being imposed on the model. Reversion of strains within the beam compromises its capacity to endure compressive actions when compared to a slab that doesn't go through it. Crushing becomes more likely after tensile cracking in previous cycles. Consequently, it is possible that the maximum moment capacity becomes closer to what is expected for the full composite section if monotonic loads are imposed instead.

On the other hand, the numerical model supports the idea that decoupling the beam and the slab (i.e. non-composite) is a sensible approach for limiting the non-linear action outside the protected zone. The moment capacity approaches the nominal capacity of the beam within the connection, even allowing for a 20% lower value for the sagging moment. This is expected as the slab offers an additional constraint for local buckling when a sagging moment is imposed, while the likelihood of out-of-plane deformation increases when compression is observed in the bottom flange when the moment reverses.

Comparatively, the best results are obtained for fully coupled RWS beam-to-column connections of 80% of the beam height, and spacings between the perforation and the column face between one perforation diameter and one time the beam height, which is in accord with specifications (Lawson



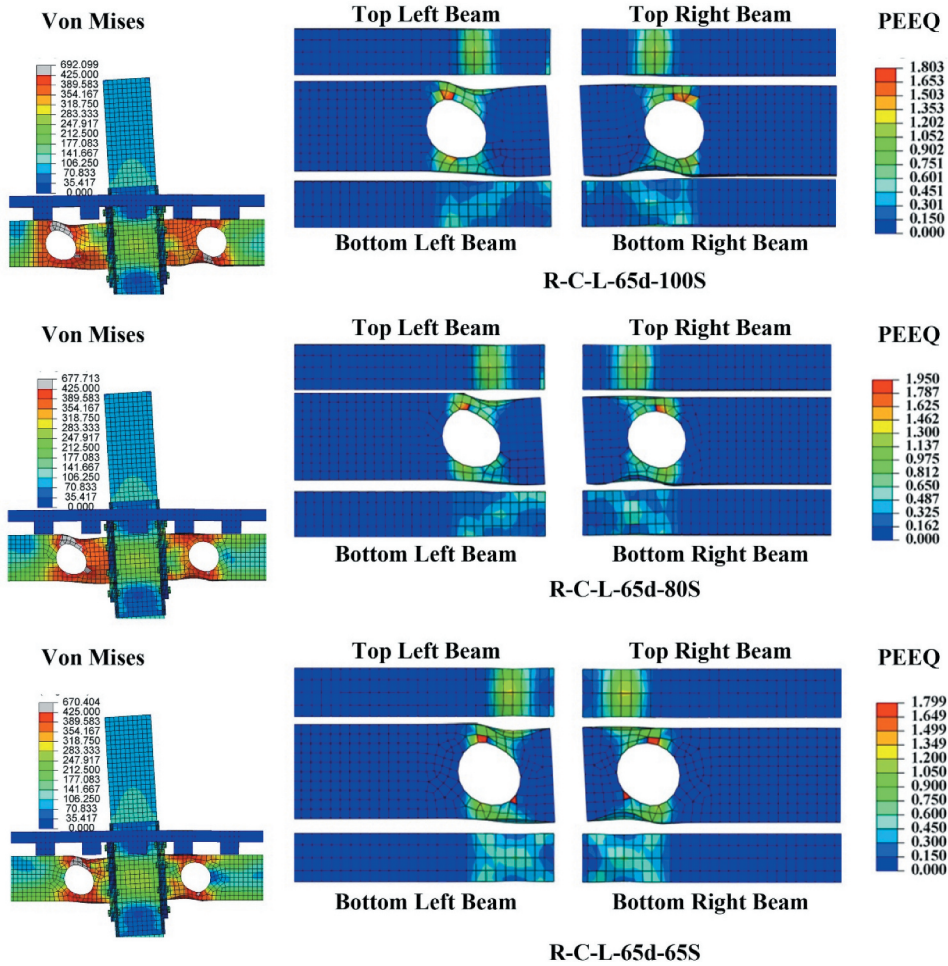


**Figure 23.** PEEQ and Von Mises stress distribution of RWS models with  $d = 0.65 h$  in the absence of shear studs over the protected zone.

and Hicks 2011). For these conditions, represented by specimens R-C-H-80-100S and R-C-H-80-80S, the connection reaches the highest ratio between the peak moment capacity and the nominal moment resistance of the bare steel section (1.48 for the sagging moment, and 1.20 for the hogging moment for the first, while 1.42 and 1.06 for the latter); being both able to accommodate 6% interstorey drifts. Although, resistance is not symmetrical, differences among sagging and hogging moments are half of what is expected for the bare-steel section, allowing for a more stable behaviour when subjected to large displacement demands. This is particularly relevant for the retrofitting of new buildings as decoupling of slabs and beams could be avoided, focusing instead on making isolated perforations on the beam's web, near beam-column interfaces. This will reduce costs and speed up work.

The advantages of limiting composite action only to the protected zone are not clear in terms of diminishing concrete cracking. Results indicate that despite this course of action, tensile cracking on the slab is as extensive as to what is observed for the fully composite action, but the maximum achieved moments are lower. Clearly, studs outside the protected zone induce at least partial strain compatibility between the slab and the beam; which leads to this undesired outcome. Also, complete avoidance of composite action is feasible, as done with other structural engineering solutions (Lee

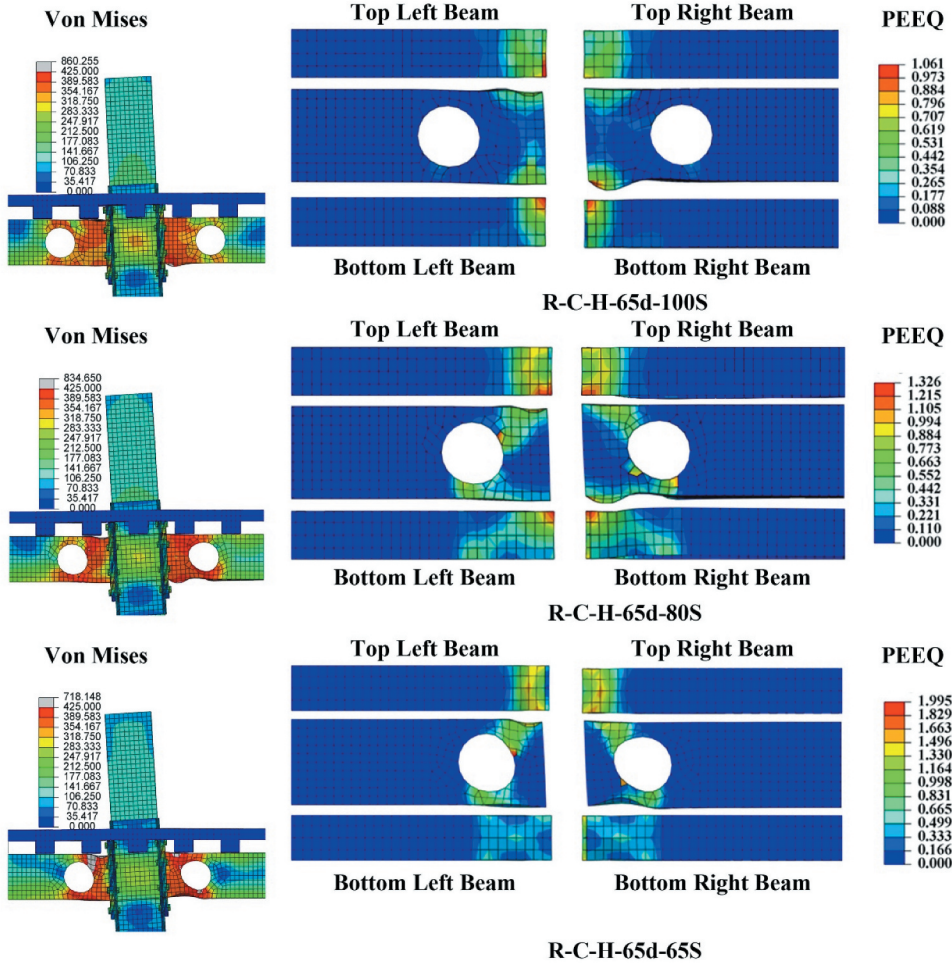


**Figure 24.** PEEQ and Von Mises stress distribution of RWS models with  $d = 0.65 h$  in the presence of shear studs over the protected zone.

et al. 2016; Zhang and Ricles 2006a, 2006b). However, the elimination of composite action (no holding) over the plastic zone in the RWS connections, led to the standard formation of the Vierendeel mechanism, like the case of connections with bare steel beams. On the other hand, RWS connections with high composite action have shown different behaviour due to the high contribution of the composite slab to the overall strength. Hence, the use of low composite action is preferable to avoid high strain demand on the bottom flange of the beam as well as cracking and crushing of the concrete slab, whilst it does not jeopardize the strong column-weak beam paradigm, following what is observed in US Standards and practice using RBS connections.

Thus, the general rules for all types of non-dissipative connections in dissipative zones of the structure specified at (ANSI/AISC 341-16 2016) can be applied to bolted extended end-plate RWS connections as follows:

$$M_{j,Rd} \geq 1.1 \cdot \gamma_{ov} \cdot (M_{pl,Rd,RWS} + V_{Ed} \cdot S) \quad (6)$$

Where  $M_{j,Rd}$  is the design resistance of the joint,  $\gamma_{ov} = 1.25$  (the overstrength factor),  $V_{Ed}$  is the shear force corresponding to the formation of a plastic hinge in the connected beam,  $S$  is the end distance between the connection face and the centerline of the web opening.

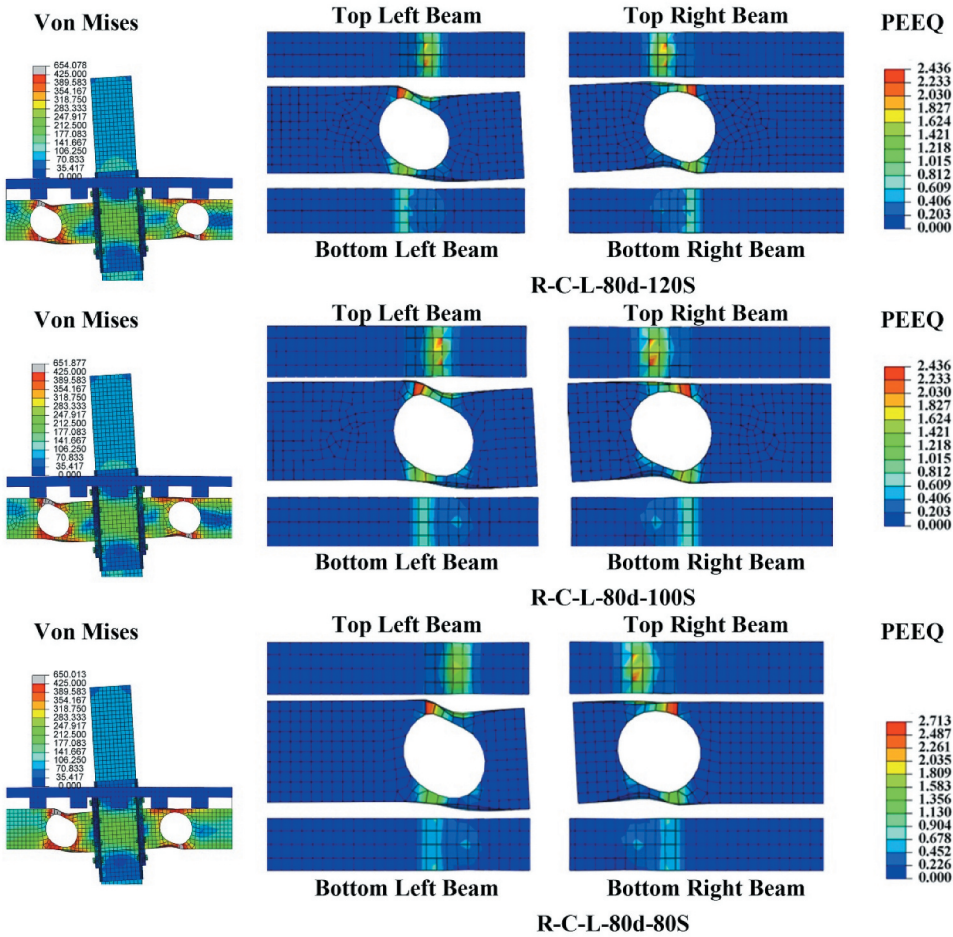


**Figure 25.** PEEQ and Von Mises stresses distribution of RWS models with  $d = 0.8 h$  in the absences of shear studs over the protected zone.

## 7. Conclusion

A high-definition finite element model was calibrated considering cyclic tests performed on full-section beams with composite slabs, designed to attain high ductility according to New Zealand Standards. The calibration of the model allowed for parametric assessments of the behaviour of composite beam-column joints with reduced web section beams. The focus was made on the diameter opening (0.8, 0.65, and 0.5 times the beam height); the distance from its centre to the column face (1.2, 1.0, 0.8, and 0.5 times the beam height) and the absence and presence of composite action over the protected zone.

All assessed specimens achieved an interstorey drift of 4%, showcasing stable hysteresis cycles without pinching or residual deformations in a particular direction when subjected to symmetric cyclic loads. The great majority (84%) of specimens reached an interstorey drift of 6%. Tearing of columns, joints and, beams was adverted, being the most critical failure mode, the failure of shear studs between the slab and the beam and the tearing of bolts in the end-plate connection. In certain cases, bolt failures in the end plate were observed. However, this happened for drift demands in excess



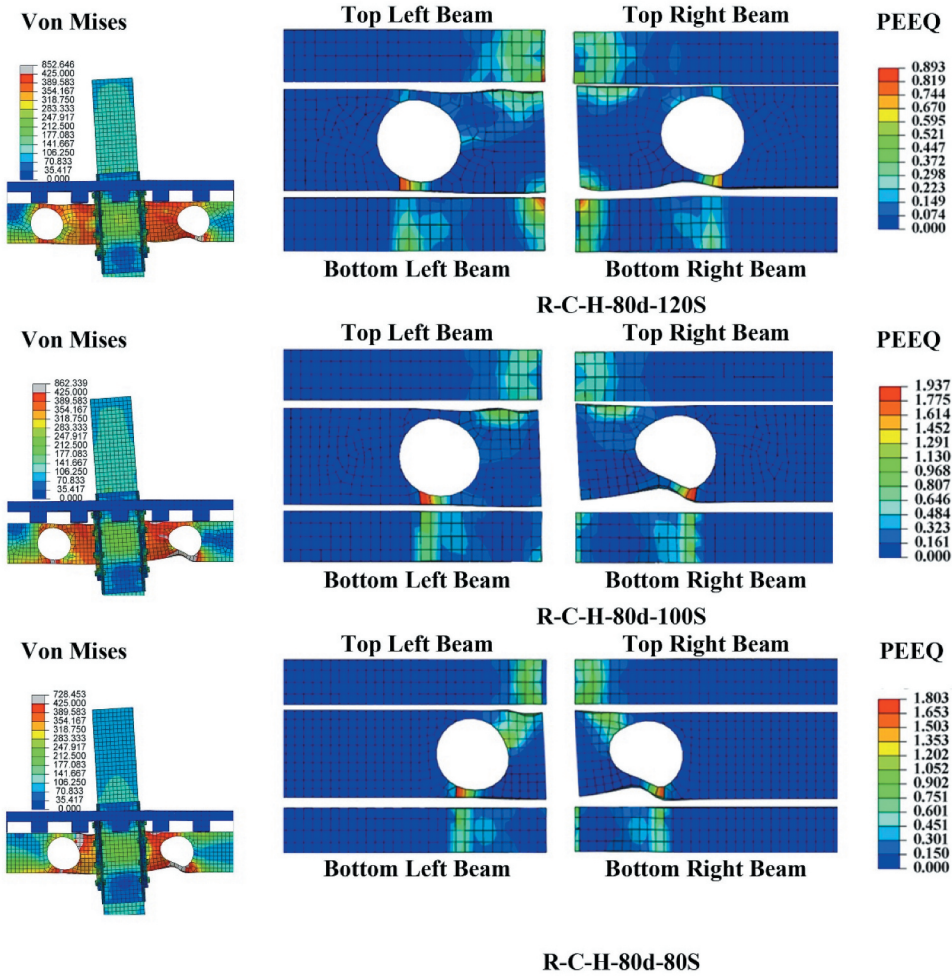


**Figure 26.** PEEQ and Von Mises stresses distribution of RWS models with  $d = 0.8 h$  in the presence of shear studs over the protected zone.

of 4%, and they could be avoided by adjusting the capacity design principles for these novel connections. Thus, they can be potentially used in special moment frames as specified in AISC 341 (2016).

The moment capacity of the full composite section ranges between 1.9 and 2 times the capacity of the bare steel section for all cases studied. The RWS connections achieved peak moment capacities significantly lower than what is expected for a connection having full composite beam-slab action. At most, the peak moment reached 1.5 times the nominal moment capacity of the bare RWS steel section ( $\frac{M_o}{M_{pl,Rd,RWS}}$ ), reaching an average of 1.36 times in specimens where the perforation was 80% of the beam's height; particularly, when full composite action was enforced for the sagging moment. For the hogging moment, values close to 1.09 times the nominal capacity are observed. When the composite action is restricted, the moment capacity ranges between 1.06 for the sagging moment and 0.9 for the hogging moment. It must be stressed that these results are observed for cyclic demands, and consequently there is a reversion of strains within the slab, which can compromise its capacity to sustain extensive compression. Contrarily, for monotonic loads, strains don't reverse within it, and consequently larger peak moments could be achieved.

## Low composite action

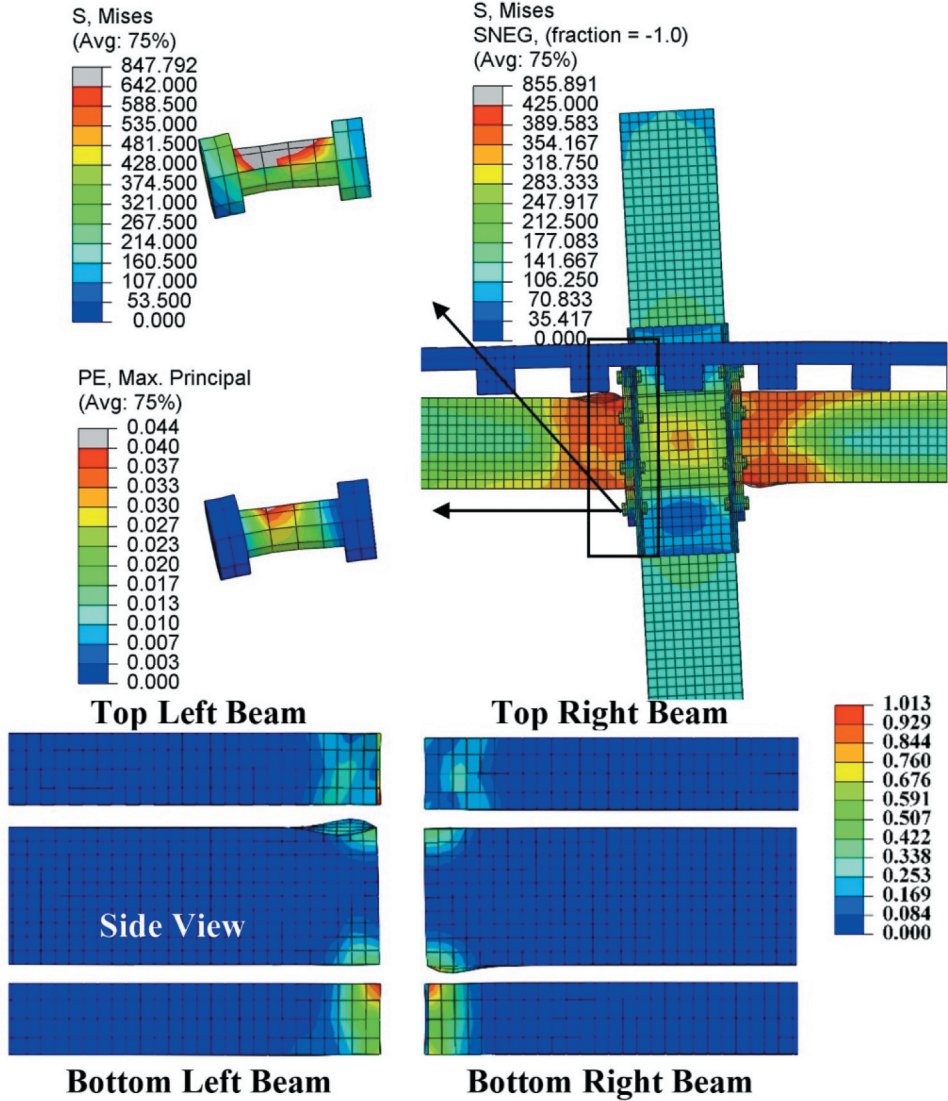


Figure 27. Distribution of PEEQ and Von Mises stresses of composite solid model (NR-C-L) in last cycle in the hysteretic curve.

Thus, numerical simulations hint that RWS connections could be an option for both retrofitting existing structures and new buildings, even when extensive deformation capacity is required. Moreover, the limited increase in moment capacity due to the slab effect indicates that the coupling of the slab and the beam have a less critical effect compared to what is observed for beams without perforations, hence providing a cap on overstrength phenomena. This is highly desirable for retrofitting existing structures where decoupling of both the slab and the beam could not be feasible. Based on this study, the design of a composite bolted extended endplate RWS connections for rehabilitation or a new seismic connection should be based on the nominal plastic bending capacity of the reduced steel beam  $M_{pl,Rd,RWS}$ , similar to what is observed for the design of the RBS connection.

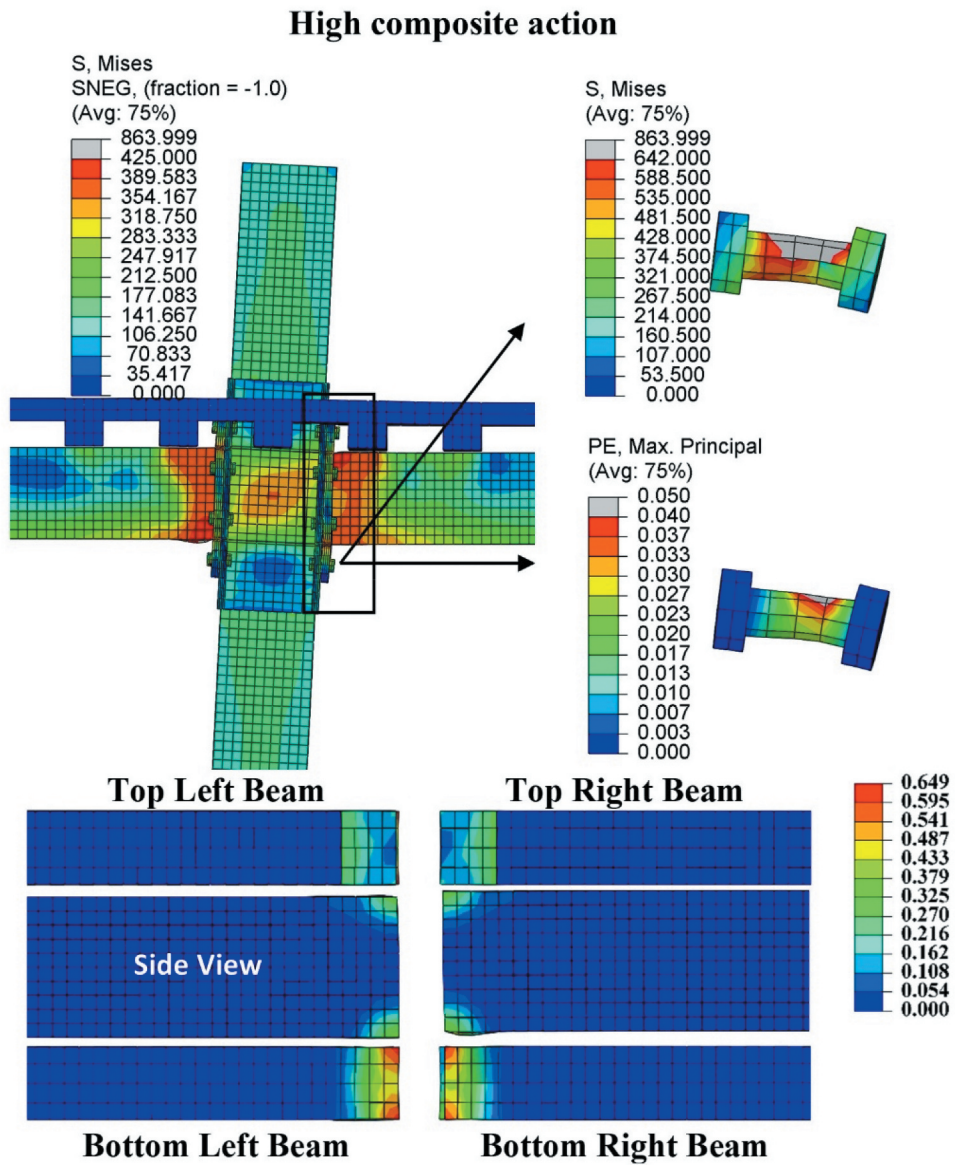


Figure 28. Distribution of PEEQ and Von Mises stresses of composite solid model (NR-C-H) in last cycle in the hysteretic curve.



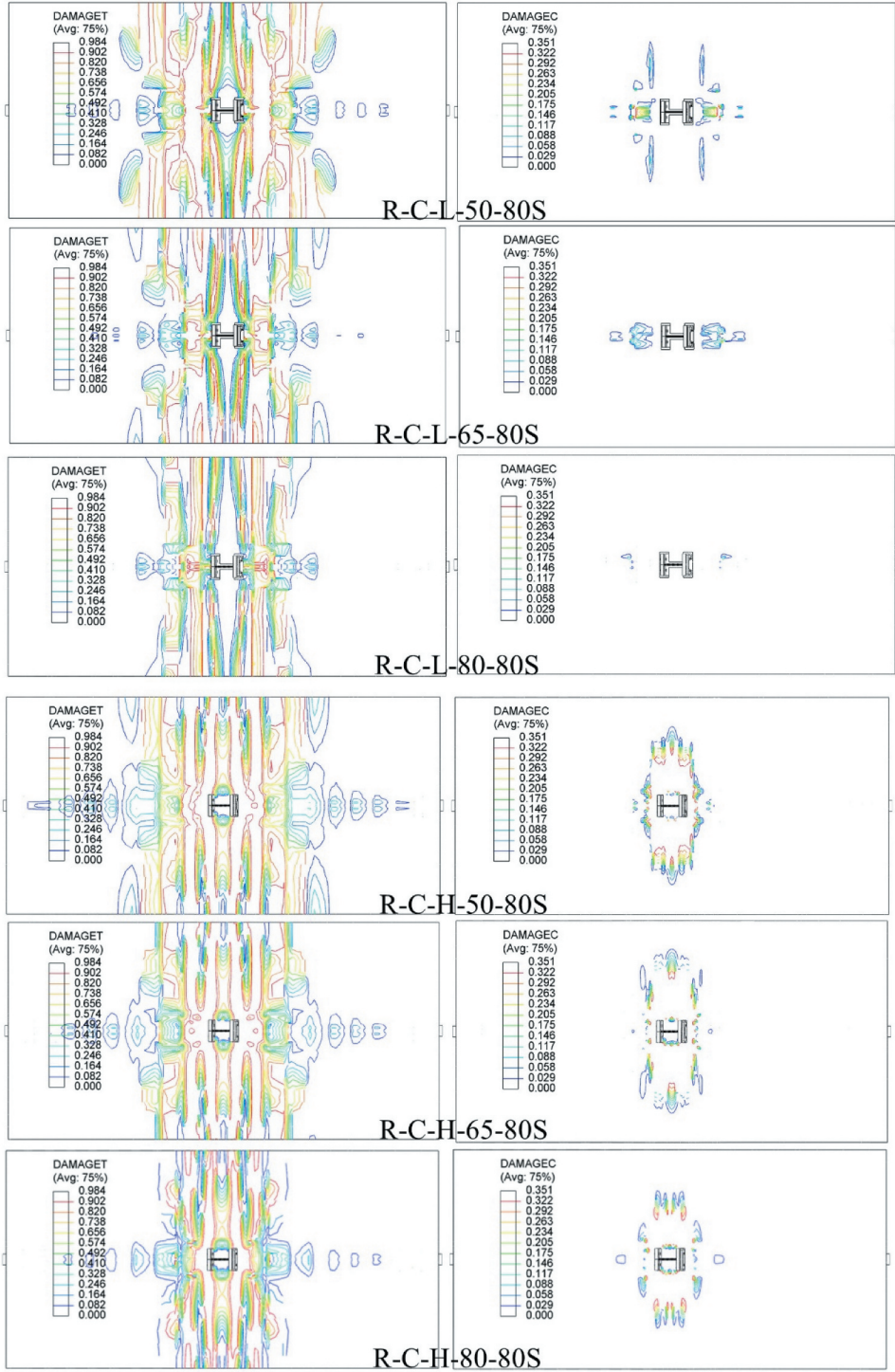
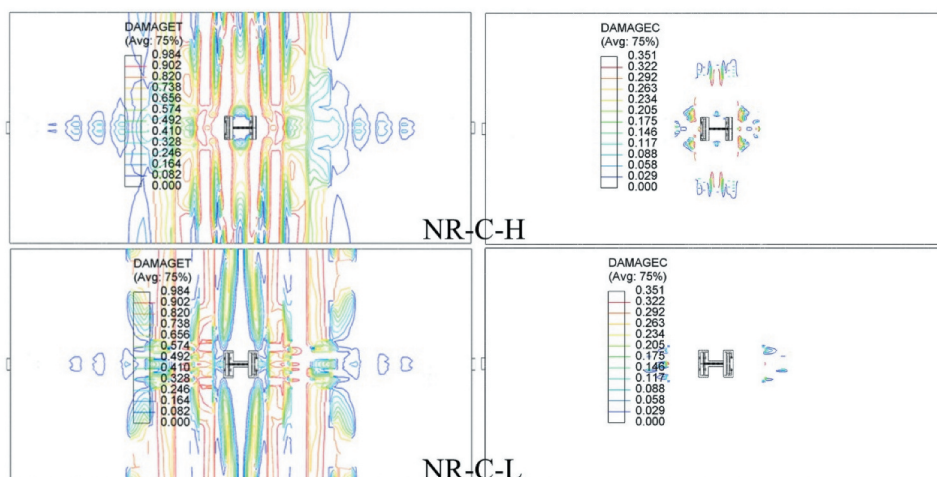


Figure 29. Concrete slab cracking and crushing in RWS models.



**Figure 30.** Concrete slab cracking and crushing in solid models.

## Disclosure Statement

No potential conflict of interest was reported by the author(s).

## Funding

Support for this work was provided by the IMAWARE initiative, which is funded by the Economic and Social Research Council of the UK (Grant number: ES/T003537/1).

## References

- ACI. 2005. ACI T1.1-01: Acceptance criteria for moment frames based on structural testing and commentary. *ACI* 374:1–5.
- Ahmed, I. M., and K. D. Tsavdaridis. 2022. Shear connection of prefabricated ultra-lightweight concrete slab systems (PUSSTM). *Structures* 36:65–97. doi:10.1016/j.istruc.2021.11.017.
- ANSI/AISC 341-16. 2016. Seismic provisions for structural steel buildings. *Seismic Provisions for Structural Steel Buildings* 60601.
- ANSI/AISC 358-16. 2016. Prequalified connections for special and intermediate steel moment frames for seismic applications.
- Baskar, K., N. E. Shanmugam, and V. Thevendran. 2002. Finite-element analysis of steel–concrete composite plate girder. *Journal of Structural Engineering* 128 (9):1158–68. doi:10.1061/(ASCE)0733-9445(2002)128:9(1158).
- Bi, R., L. Jia, P. Li, and Q. Wang. 2021. Multiparameter seismic behavior of castellated beam-to-column connections based on stress migration. *Structures* 29:1137–53. doi:10.1016/j.istruc.2020.12.016.
- Boushehri, K., D. Tsavdaridis, and G. Cai. 2019. Seismic behaviour of RWS moment connections to deep columns with European sections. *Journal of Constructional Steel Research* 161:416–35. doi:10.1016/j.jcsr.2019.07.009.
- Chaudhari, T. 2017. *Seismic performance evaluation of steel frame building with different composite slab configurations*. PhD Thesis, University of Canterbury, Christchurch, NZ.
- Chaudhari, T., G. MacRae, D. Bull, C. Clifton, and S. Hicks. 2019. Experimental behaviour of steel beam-column subassemblies with different slab configurations. *Journal of Constructional Steel Research* 162:105699. doi:10.1016/j.jcsr.2019.105699.
- Chen, S.-J., and Y. C. Chao. 2001. Effect of composite action on seismic performance of steel moment connections with reduced beam sections. *Journal of Constructional Steel Research* 57 (4):417–34. doi:10.1016/S0143-974X(00)00022-5.
- Civjan, S. A., M. D. Engelhardt, and J. L. Gross. 2000. Retrofit of pre-Northridge moment-resisting connections. *Journal of Structural Engineering* 126 (4):445–52. doi:10.1061/(ASCE)0733-9445(2000)126:4(445).
- Civjan, S. A., M. D. Engelhardt, and J. L. Gross. 2001. Slab effects in SMRF retrofit connection tests. *Journal of Structural Engineering* 127 (3):230–37. doi:10.1061/(ASCE)0733-9445(2001)127:3(230).



- Cornelissen, H. A. W., D. A. Hordijk, and H. Reinhardt. 1986. Experimental determination of crack softening characteristics of normalweight and lightweight. *Heron* 31 (2):45–56.
- Darwin, D., and R. C. Donahey. 1988. LRFD for composite beams with unreinforced web openings. *Journal of Structural Engineering* 114 (3):535–52. doi:10.1061/(ASCE)0733-9445(1988)114:3(535).
- Dassault Systemes. 2014. *ABAQUS user subroutines reference guide V. 6.14*. Providence, RI, USA: Dassault Systemes, Simulia Corporation.
- Davarpanah, M., H. Ronagh, P. Memarzadeh, and F. Behnamfar. 2020. Cyclic behavior of welded elliptical-shaped RWS moment frame. *Journal of Constructional Steel Research* 175:106319. doi:10.1016/j.jcsr.2020.106319.
- Díaz, C., M. Victoria, P. Martí, and O. M. Querin. 2011. FE model of beam-to-column extended end-plate joints. *Journal of Constructional Steel Research* 67 (10):1578–90. doi:10.1016/j.jcsr.2011.04.002.
- Díaz, C., M. Victoria, O. M. Querin, and P. Martí. 2018. FE model of three-dimensional steel beam-to-column bolted extended end-plate joint. *International Journal of Steel Structures* 18 (3):843–67. doi:10.1007/s13296-018-0033-y.
- ElSabbagh, A., T. Sharaf, S. Nagy, and M. ElGhandour. 2019. Behavior of extended end-plate bolted connections subjected to monotonic and cyclic loads. *Engineering Structures* 190:142–59. doi:10.1016/j.engstruct.2019.04.016.
- Erfani, S., and V. Akrami. 2017. Increasing seismic energy dissipation of steel moment frames using reduced web section (RWS) connection. *Journal of Earthquake Engineering* 21 (7):1090–112. doi:10.1080/13632469.2016.1210057.
- Erfani, S., V. Akrami, and A. Mohammad-Nejad. 2020. Lateral load resisting behavior of steel moment frames with reduced web section (RWS) beams. *Structures* 28:251–65. doi:10.1016/j.istruc.2020.08.060.
- Eurocode. 2004. Eurocode 2: Design of concrete structures—part 1.1: General rules and rules for buildings. European Commission Standardization, Brussels, Belgium.
- Eurocode. 2005a. Eurocode 3: Design of steel structures—Part 1–8: Design of joints—the European Standard EN 1993-1-8: 2005. European Commission Standardization, Brussels, Belgium (1993).
- Eurocode. 2005b. Eurocode 3: Design of steel structures—Part 1-1: General rules and rules for buildings. European Commission Standardization, Brussels, Belgium (1993).
- Eurocode. 2005c. Eurocode 4. Design of composite steel and concrete structures. Part 1.1: General rules and rules for buildings. European Commission Standardization, Brussels, Belgium (1994).
- Eurocode. 2005d. Eurocode 8: Design of structures for earthquake resistance—Part 1: General rules, seismic actions and rules for buildings. European Commission Standardization, Brussels, Belgium (1998).
- Gerami, M., H. Saberi, V. Saberi, and A. S. Daryan. 2011. Cyclic behavior of bolted connections with different arrangement of bolts. *Journal of Constructional Steel Research* 67 (4):690–705. doi:10.1016/j.jcsr.2010.11.011.
- Gil, B., R. Goñi, and E. Bayo. 2013. Experimental and numerical validation of a new design for three-dimensional semi-rigid composite joints. *Engineering Structures* 48:55–69. doi:10.1016/j.engstruct.2012.08.034.
- Guo, B., J. T. Wang, T. Liang, and Z. Bao. 2011. Study on seismic performance of a new type energy dissipation steel moment frames. *Applied Mechanics and Materials* 94–96:764–70. doi:10.4028/000http://www.scientific.net/AMM.94-96.764.
- Jones, S. L., G. T. Fry, and M. D. Engelhardt. 2002. Experimental evaluation of cyclically loaded reduced beam section moment connections. *Journal of Structural Engineering* 128 (4):441–51. doi:10.1061/(ASCE)0733-9445(2002)128:4(441).
- Kim, S.-Y., and C.-H. Lee. 2017. Seismic retrofit of welded steel moment connections with highly composite floor slabs. *Journal of Constructional Steel Research* 139:62–68. doi:10.1016/j.jcsr.2017.09.010.
- Lam, D. and F. Fu. 2005. Modelling of semi-rigid composite beam-column connections with precast hollow core slabs. In *Fourth International Conference on Advances in Steel Structures*, June 13–15, Shanghai, China, 787–92.
- Landolfo, R., F. M. Mazzolani, D. Dubina, L. S. da Silva, and M. D’Aniello. 2017. Design of steel structures for buildings in seismic areas: Eurocode 8: Design of steel structures in seismic areas. General rules and rules for buildings.
- Lawson, R. M. and S. J. Hicks. 2011. Design of composite beams with large web openings. *SCI P355*.
- Lee, C. H., J. H. Jung, S. Y. Kim, and J. J. Kim. 2016. Investigation of composite slab effect on seismic performance of steel moment connections. *Journal of Constructional Steel Research* 117:91–100. doi:10.1016/j.jcsr.2015.10.004.
- Lim, C., W. Choi, and E. A. Sumner. 2012. Low cycle fatigue life prediction using a four-bolt extended unstiffened end plate moment connection. *Engineering Structures* 41:373–84. doi:10.1016/j.engstruct.2012.03.039.
- Li, B., Q. Yang, and N. Yang. 2011. An investigation on a seismic connection with opening in beam web in steel moment frames. *Advances in Structural Engineering* 14 (3):575–87. doi:10.1260/1369-4332.14.3.575.
- Mashaly, E., M. El-Hewity, H. Abou-Elfath, and M. Osman. 2011. Behavior of four-bolt extended end-plate connection subjected to lateral loading. *Alexandria Engineering Journal* 50 (1):79–90. doi:10.1016/j.aej.2011.01.011.
- Momenzadeh, S., M. T. Kazemi, and M. H. Asl. 2017. Seismic performance of reduced web section moment connections. *International Journal of Steel Structures* 17 (2):413–25. doi:10.1007/s13296-017-6004-x.
- Morrison, M., S. Quayyum, and T. Hassan. 2017. Performance enhancement of eight bolt extended end-plate moment connections under simulated seismic loading. *Engineering Structures* 151:444–58. doi:10.1016/j.engstruct.2017.08.040.
- Morrison, M. L., D. Q. Schweizer, and T. Hassan. 2016. Seismic enhancement of welded unreinforced flange-bolted web steel moment connections. *Journal of Structural Engineering* 142 (11):4016102. doi:10.1061/(ASCE)ST.1943-541X.0001575.

- Naughton, D. T., K. D. Tsavdaridis, C. Maraveas, and A. Nicolaou. 2017. Pushover analysis of steel seismic resistant frames with reduced web section and reduced beam section connections. *Frontiers in Built Environment* 3:59. doi:10.3389/fbuil.2017.00059.
- Nazaralizadeh, H., H. Ronagh, P. Memarzadeh, and F. Behnamfar. 2020. Cyclic performance of bolted end-plate RWS connection with vertical-slits. *Journal of Constructional Steel Research* 173:106236. doi:10.1016/j.jcsr.2020.106236.
- Shaheen, M. A., K. D. Tsavdaridis, and S. Yamada. 2018. Comprehensive FE study of the hysteretic behavior of steel-concrete composite and noncomposite RWS beam-to-column connections. *Journal of Structural Engineering* 144 (9). doi:10.1061/(ASCE)ST.1943-541X.0002124.
- Shin, M., S. -P. Kim, A. Halterman, and M. Aschheim. 2017a. Seismic toughness and failure mechanisms of reduced web-section beams: Phase 1 tests. *Engineering Structures* 141:198–216. doi:10.1016/j.engstruct.2017.03.016.
- Shin, M., S. -P. Kim, A. Halterman, and M. Aschheim. 2017b. Seismic toughness and failure mechanisms of reduced web-section beams: Phase 2 tests. *Engineering Structures* 141:607–23. doi:10.1016/j.engstruct.2017.03.046.
- Sofias, C. E., C. N. Kalfas, and D. T. Pachoumis. 2014. Experimental and FEM analysis of reduced beam section moment endplate connections under cyclic loading. *Engineering Structures* 59:320–29. doi:10.1016/j.engstruct.2013.11.010.
- Standards New Zealand. 2007. NZS 3404 Part 1: 1997 Steel Structures Standard. Standards New Zealand, Wellington, NZ.
- Sumner, E. A. 2003. Unified design of extended end-plate moment connections subject to cyclic loading. PhD Thesis, Virginia Tech, Blacksburg, VA, USA.
- Sumner, E. A., T. W. Mays, and T. M. Murray. 2000a. Cyclic testing of bolted moment end-plate connections. Research report SAC/BD-00/21. CE/VPI-ST 00/03.
- Sumner, E. A., T. W. Mays, and T. M. Murray. 2000b. End-plate moment connections: Test results and finite element method validation. In *Connections in Steel Structures IV: Steel Connections in the New Millennium: Proceedings of the Fourth International Workshop*, Roanoke, VA, October 22–25.
- Tabar, A. M., A. Alonso-Rodríguez, and K. D. Tsavdaridis. 2022. Building retrofit with reduced web (RWS) and beam (RBS) section limited-ductility connections. *Journal of Constructional Steel Research* 197:107459. doi:10.1016/j.jcsr.2022.107459.
- Tsavdaridis, K. D. and C. D'Mello. 2009. FE investigation of perforated sections with standard and non-standard web opening configurations and sizes. In *6th International Conference on Advances in Steel Structures*, Hong Kong, China, December 16–18 Dec.
- Tsavdaridis, K. D., F. Faghil, and N. Nikitas. 2014. Assessment of perforated steel beam-to-column connections subjected to cyclic loading. *Journal of Earthquake Engineering* 18 (8):1302–25. doi:10.1080/13632469.2014.935834.
- Tsavdaridis, K. D., C. K. Lau, and A. Alonso-Rodríguez. 2021. Experimental behaviour of non-seismical RWS connections with perforated beams under cyclic actions. *Journal of Constructional Steel Research* 183:106756. doi:10.1016/j.jcsr.2021.106756.
- Tsavdaridis, K. D., and T. Papadopoulos. 2016. A FE parametric study of RWS beam-to-column bolted connections with cellular beams. *Journal of Constructional Steel Research* 116:92–113. doi:10.1016/j.jcsr.2015.08.046.
- Vasdravellis, G., M. Valente, and C. A. Castiglioni. 2009. Behavior of exterior partial-strength composite beam-to-column connections: Experimental study and numerical simulations. *Journal of Constructional Steel Research* 65 (1):23–35. doi:10.1016/j.jcsr.2008.01.034.
- Wang, A. J. 2010. Numerical studies on the structural behaviour of composite end-plate connections. *Canadian Journal of Civil Engineering* 37 (6):907–21. doi:10.1139/L10-045.
- Wang, J., B. Uy, H. -T. Thai, and D. Li. 2018. Behaviour and design of demountable beam-to-column composite bolted joints with extended end-plates. *Journal of Constructional Steel Research* 144:221–35. doi:10.1016/j.jcsr.2018.02.002.
- Yang, Q., B. Li, and N. Yang. 2009. Aseismic behaviors of steel moment resisting frames with opening in beam web. *Journal of Constructional Steel Research* 65 (6):1323–36. doi:10.1016/j.jcsr.2009.01.007.
- Zhang, X., and J. M. Ricles. 2006a. Experimental evaluation of reduced beam section connections to deep columns. *Journal of Structural Engineering* 132 (3):346–57. doi:10.1061/(ASCE)0733-9445(2006)132:3(346).
- Zhang, X., and J. M. Ricles. 2006b. Seismic behavior of reduced beam section moment connections to deep columns. *Journal of Structural Engineering* 132 (3):358–67. doi:10.1061/(ASCE)0733-9445(2006)132:3(358).
- Zhang, X., S. Zheng, and X. Zhao. 2019. Seismic performance of steel beam-to-column moment connections with different structural forms. *Journal of Constructional Steel Research* 158:130–42. doi:10.1016/j.jcsr.2019.03.028.